Shock Ignition of Particles

Frolov S. M.[1] and Fedorov A. V.[2]
[1]*Semenov Institute of Chemical Physics, Moscow, Russia*
[2]*Institute for Theoretical and Applied Mechanics, Novosibirsk, Russia*

Contents

Nomenclature

A particle/drop cross-section area
a small half-axis of ellipsoid
a_d drop acceleration
B mass transfer coefficient
b large half-axis of ellipsoid
C concentration
c specific heat
c_p specific heat at constant pressure
C_D aerodynamic drag coefficient
D binary diffusion coefficient
D SW velocity
d_s particle/drop diameter
E activation energy
F_B Basset force
F_m Force of virtual masses
F_S Stokes force
$Fo = at / r_{s0}$
h oxide film thickness
I_j normalized mass content of the jth species in gas phase
j mass flow rate
K preexponential factor
k_0 preexponential factor
k_h heat transfer coefficient
L latent heat of vaporization
Le Lewis number
M Mach number
M number of species in gas phase
m particle/drop mass
n reaction order
Nu Nusselt number
Oh Ohnesorge number
Pr Prandtl number
p pressure
Q heat flux
q chemical reaction heat
R gas constant
R_c half-distance between particles in the suspension
R_{sc} radius of spherical elementary cell
Re Reynolds number
r radial coordinate
r_s particle/drop radius
S particle/drop surface area
S_c surface area of polygonal elementary cell
S_{sc} surface area of spherical elementary cell
T mean particle/drop temperature
T_M reference temperature
T_m boiling temperature
$T'_{\max}$ maximal rate of temperature rise
$\tilde{T}$ gas temperature
$\tilde{T}_1$ gas temperature behind reflected SW
$\tilde{T}_*$ reference temperature
$\tilde{T}_{\lim}$ minimal temperature of the oxidizing medium required for particle ignition
t time
t_{ign} ignition delay time
t_l drop lifetime
t_{cf} ignition delay of cool flame
t_h characteristic heating time of particle/drop
t^* dimensionless drop breakup tiime
V particle/drop volume
V_c volume of polygonal elementary cell
V_{sc} volume of spherical elementary cell
v reference rate of vaporization
U relative velocity of gas and particle/drop
u velocity
x coordinate
Y_j gaseous species mass fraction
y dimensionless drop deformation

Greek symbols

ε particle blackness rate
Δ drop deformation degree
δ displacement of the drop equator
λ thermal conductivity
λ_w wavelength of instability wave
μ viscosity
η mass content of liquid in the unit volume of drop suspension
ρ density
σ Stefan–Boltzmann constant

σ_l	liquid surface tension
ϕ_{st}	stoichiometric ratio
Φ	fuel–air ratio
τ_{vel}	characteristic time of particle/drop velocity relaxation
ψ	function
θ, θ_f	heat transfer intensification coefficients
κ	temperature diffusivity

Indices

0	initial value
∞	relates to large distance from particle/drop
a	refers to ambient conditions
eff	effective value
g	relates to gas
i	relates to particle/drop surface
l	relates to liquid
max	maximal value
ox	relates to oxide film
s	relates to solid
v	relates to fuel vapor
vd	relates to fuel initially in liquid phase
vg	relates to prevaporized fuel
wb	relates to wet-bulb temperature

Introduction

Ignition and combustion of fine solid particles and liquid fuel drops (particles, for short) are the issues important for various branches of science and technology, such as aerospace and chemical technologies, chemical propulsion, ground transportation, and industrial safety. These issues called attention of numerous researchers both at the end of the foregoing century and at present, and many relevant publications are available in literature. Detailed reviews of the current status of the research can be found elsewhere [1–5].

Particle ignition and combustion are the phenomena comprising all main constituents of the combustion process, namely, fast exothermic chemical reactions complicated by diffusion of reactants and products, thermal energy deposition and spreading of heat in the medium, and convective flows. The classical theory implies that particle combustion is diffusion limited and therefore chemical kinetic aspects are usually out of the analysis [6–15]. In addition, the classical theory considers an isolated particle in unconfined ambience. Within these presumptions, notable progress in understanding relevant physical and chemical processes has been achieved recently. However, for problems dealing with transient modes of combustion, like ignition or extinction, it is necessary to consider the effects of finite-rate chemical kinetics. Moreover, in practice, particle ignition and combustion occur in presence of neighboring particles or confinement surfaces. The corresponding effects are usually referred to as ‘spray’ (or ‘collective’) and ‘confinement’ effects.

Spray effects manifest themselves in two-phase reactive flows. In existing computational approaches, chemical reaction rates are determined based on considering particles as distributed mass, momentum, and energy sources. As a matter of fact, spray ignition and combustion phenomena are a complex combination of chemical kinetics and diffusion-controlled flames around individual particles, their groups, and gas-phase partially premixed flames.

For modeling ignition and combustion of particles in sprays and clouds, several approaches are used by analyzing the evolution of (*i*) two or more particles [16, 17], (*ii*) a regular sequence of particles [18, 19], (*iii*) a group of chaotically distributed particles [20, 21], or (*iv*) particle suspension [22]. Advantages and drawbacks of these approaches are discussed elsewhere [2–7]. Note only that the most detailed description of the flow fields in the space between particles has been obtained in the analysis of two interacting particles and the linear array of particles. “Group” and “suspension” theories do not take into account transient heat and mass transfer processes in particle vicinity, as well as the dependence of the rates of these processes on the distance between particles.

At present, ignition and combustion of particles in combustion chambers are modeled without regard for many factors affecting both local and integral combustor performance. Dynamic and thermal effects of particles on the flow are modeled in terms of the averaged interphase mass, momentum and energy fluxes [22]. Effect of turbulence on phase interaction is modeled by turbulent dispersion of particles [5]. Mixing of gas-phase species (vapors and reaction products) is

modeled by micromixing models which do not account for the difference in species diffusion coefficients. Finite instantaneous depths of penetration of heat and diffusion fluxes from each individual particle are also not taken into account. As a matter of fact, in computational algorithms, the increments of thermal energy and gas-phase species mass arising due to particle or drop ignition and combustion are smeared uniformly throughout a corresponding computational cell, despite the cell size is usually several orders of magnitude larger than the characteristic particle size. As a consequence, gas-phase chemical processes (intrinsically local) are treated as volumetric. In view of it, a computational cell size becomes an important artificial parameter of a problem solved. Its value determines the dynamics of local and integral phenomena studied. However, particles are known to be surrounded by finite-dimension spatial regions with highly nonuniform distributions of temperature and species concentrations. The dimensions of such regions depend on time and instantaneous mutual position of neighboring particles. In such conditions, preignition processes as well as ignition and combustion cannot be considered as processes in a well-stirred reactor represented by a computational cell.

In this paper we concentrate on fundamental issues of shock-induced particle and drop ignition and overview the problems of adequate mathematical modeling of relevant phenomena. Subsequent stages of ignition process development (combustion, extinction, etc.) are out of the scope of this paper. As examples of solid particles, magnesium (Mg) and aluminum (Al) are mainly considered. Their oxidation rates either depend on the oxide film thickness (Al) or independent of it (Mg). As examples of liquid fuel drops, single-component *n*-alkane drops are considered.

1. Ignition of solid particles

1.1 Experimental and theoretical findings

Ignition of solid particles in a high-temperature gas flow behind a shock wave (SW) propagating in gas–particle suspension was studied experimentally elsewhere [23–47]. Figure 1 shows a typical schematic of experimental conditions in a shock tube [46, 47]: a) before firing; b) after firing, but before the SW has reached the end wall; and c) after SW reflection. In the experiments on particle ignition behind incident SW, Region 2 is the test region. If particle ignition is studied behind reflected SW, Region 5 serves as the test region. Pressure and temperature in Regions 2 and 5 are set by adjusting the initial conditions in the driver section (Region 4) and driven section (Region 1) of the shock tube before firing and by monitoring SW velocity along the tube in the course of experiments. To estimate the conditions of experiments, ideal compressible gas relations and Rankine–Hugoniot relationships are usually used.

The shock tube can be either vertical or horizontal. Vertical shock tubes have the advantage of creating dust suspensions, which are homogeneous in tube cross-section. However, gravitational dust sedimentation can lead to dust density variation along the tube. To avoid the effect of sedimentation, various techniques of dust dispersion are used. For example, in [24, 32, 37, 47], dust powders were mounted on a horizontal shelf or knife blade, at a short distance from the end wall. The incident SW swept over the particles, entraining them in the postshock flow and thus creating a particle suspension. After the SW reflected off the end wall, the particles in suspension were heated and ignited if the temperature, pressure, and composition conditions behind the reflected SW were appropriate for ignition.

Figure 2 shows a typical flow field wave diagram for the shock tube near the end wall, with axial position on the horizontal axis and time on the vertical axis [46, 47]. The incident SW first approaches and then reflects from the end wall, positioned on the right side of the *x*-axis. Then the reflected SW moves away from the end wall until it reaches the contact surface, which is moving toward the end wall at the same velocity as the gas in Region 2. Through this interaction, a normal shock is transmitted through the contact surface, moving away from the end wall, and a SW, Mach wave, or expansion wave, depending on the thermodynamic properties of the gases in Regions 2 and 3, is reflected back toward the end wall. This wave then returns to the end wall and reflects from it, ending the test period. The gas in Region 5 is a stagnant, hot, high-pressure mixture in which solid particles are ignited. Thus, the test time is the time between the arrival of the incident

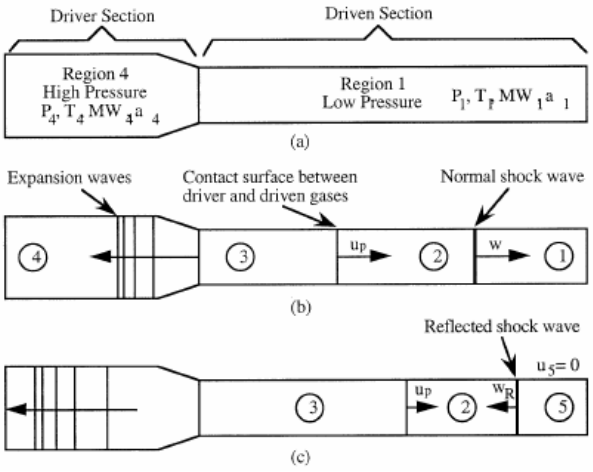

Figure 1: Typical schematic of experimental conditions in a shock tube [46, 47]: (*a*) before firing of the tube; (*b*) after firing, but before reflection of the incident shock wave; and (*c*) after reflection of the incident shock wave from end wall.

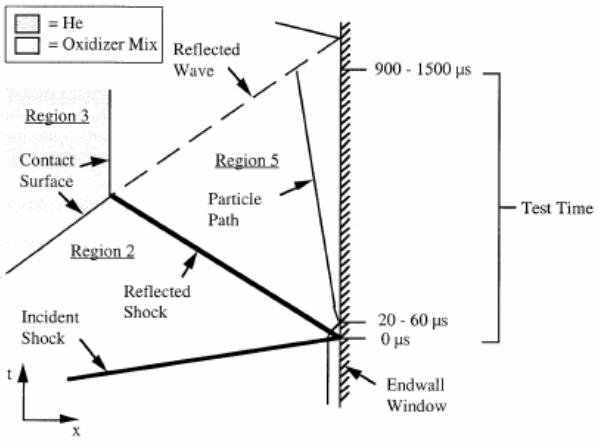

Figure 2: Flow field in time (*t*) – distance (*x*) coordinates near the shock-tube end wall showing flow interactions and particle position vs. time [46, 47].

SW at the end wall and the arrival of the wave reflected from the contact surface at the drifting particles. In experiments [46, 47], test time ranged from 900 to 1500 μs.

The experimental data on the ignition delay time t_{ign} as a function of the initiating SW Mach number M_0 are available for various metals: volatile (magnesium, zinc, etc.), intermediate (aluminum, iron, copper, lead, titanium, hafnium, etc.), and refractory (tantalum, tungstem, niobium); nonmetallic inorganic elements (boron, silicon, carbon, etc.); various organic dusts (cornstarch, wheaten flour, etc.), and monopropellants and high explosives (RDX, TNT, etc.).

For a suspension of Mg particles of mean initial radius $r_{s0} = 17$ μm, the dependence of t_{ign} on postshock temperature T_0 was obtained, for example, in [27]. At temperatures T_0 = 1538–2500 K, the ignition delay time of Mg particles varied from 0.1 to 0.05 ms.

For a suspension of fine Al particles ($r_{s0} = 5$–10 μm), the $t_{ign}(T_0)$ dependence was obtained, for example, in [47]. Al particles were ignited in atmospheres consisting of Ar and varying amounts of H_2O, CO_2, and O_2 at the end wall of a shock tube. At pressures and temperatures of about 0.85 MPa and 2600 K, the measured ignition delays were in the range from 150 to 900 μs. Interestingly, Al particles ignited in a mixture of H_2O/Ar showed ignition delay times 3 to 6 times greater than those from CO_2/O_2/Ar mixtures.

In the literature, there are still inconsistencies in available experimental data. For example, in some experimental studies the ignition delays were found to reduce when the measurements were made behind reflected SW rather than behind incident SW [36, 37]. In other studies (e.g., [30, 34, 35, 41] some dusts were more easily ignited behind incident SW than behind reflected SW.

Experimental studies of combustion of various metal particles [48–58] indicate the important role of heterogeneous reactions. It is known that during the oxidation of metal particles in a gaseous oxidizer, an oxide film separates the metal and oxidizer. The rate of reaction is then governed by the protective properties of this film. In [8, 9], this implication was used to model ignition of individual metal particles in a high-temperature oxidizing atmosphere. Particle ignition was found to occur due to thermal breakdown, when the rate of heat evolution during oxidation becomes larger than the rate of heat removal from the particle surface.

Ignition of volatile metals, due to their low boiling points (~ 1360 K for Mg), can occur in a vapor phase according to [6]. However, metal oxide layers were always observed on the surface of

particles, which indicates the significance of heterogeneous reactions during ignition [55–58]. Ignition of boron particles is inhibited by a thin layer of B_2O_3 on the particle surface, and the high vaporization temperature of boron (~ 4100 K) limits oxidation to slower heterogeneous surface reactions.

There exist a number of theoretical models of particle ignition [59–84]. In most of the models, the metal particle ignition law is represented in the form of Arrhenius expression with certain values of preexponential factor K in the oxide film growth rate and the activation energy E of the oxidation process. These kinetic constants are found by fitting experimental and theoretical dependencies of t_{ign} on M_0.

The models differ considerably by their predicting capabilities. For example, the values of t_{ign} predicted in [62] appeared to be an order of magnitude larger than the values measured in dynamic conditions behind a SW [27]. The authors of [72–77] have found the values of K and E for the dynamic model of particle ignition in the flow behind a propagating SW. They have taken particle motion and low-temperature oxidation into account. The resultant values of K and E appeared to be different from those in the static ignition model, which does not account for the relative motion of solid particles and gas.

A simple estimate for the particle velocity relaxation time, τ_{vel}, in the gas flow using the Stokes law $\tau_{\text{vel}} = (2/9)\rho_s r_{s0}^2/\mu$ shows that at $r_{s0} = 1$ and 5 μm, $\tau_{\text{vel}} = 0.02$ and 0.5 ms, respectively. Here, ρ_s is the particle material density and μ is the gas viscosity. According to the ignition delay data [63], the effect of velocity relaxation for fine particles may be insignificant at low flow velocities. The velocity of very fine particles achieves rapidly the ambient gas velocity, and the heating conditions become quickly similar to those in a quiescent atmosphere. Besides the differences in K and E values at static and dynamic conditions, there is also a considerable scatter in the values of determining parameters in available mathematical models of particle ignition. As a result, the constants in the models differ considerably, sometimes by orders of magnitude. Therefore, it is worth discussing these problems, first on the example of metal particle ignition in static conditions.

In general, all mathematical models of metal particle ignition in the quiescent atmosphere are based on two approaches [59–71]. The first approach applies the thermal explosion theory developed by Semenov. The second is based on the "reduced film" concept. The critical analysis of these approaches [78] resulted in the following findings.

(1) Two unknown constants, K and E, in the models are determined from experimental dependencies at essentially different conditions. In [59, 60], they were found for small values of r_{s0} based on the critical "breakdown" temperature of a liquid Mg particle. In [65, 66], they were found for large values of r_{s0} for solid Mg particles. As a result, the values of constants in these papers are different.

(2) Only models based on the second approach contain information on the dependence of the medium critical temperature on oxygen concentration and particle radius as well as the dependence of the ignition delay time on the particle radius.

(3) Neither of the papers cited contains a qualitative study of the solutions of the corresponding Cauchy problem for the models using the first approach or the corresponding boundary-value problem for the models using the second approach. Such mathematical issues as solvability of governing transcendental equations for determining K and E were not addressed. Moreover, no comparison of the data on the temperature growth dynamics by different models has been made [78].

1.2. Static conditions

1.2.1 General mathematical model

Consider a metal particle placed in a hot flow of oxidizing gas. It is assumed that exothermic oxidation reaction and endothermic phase transition (melting, vaporization, etc.) take place on the

particle surface. The particle is assumed to occupy region Ω in the space with Cartesian coordinates (x_1, x_2, x_3). The mathematical model governing evolution of the temperature field in the particle is based on the energy conservation equation [85]:

$$c_s \rho_s \frac{\partial T}{\partial t} = \lambda_s \Delta T, \quad t > 0, \quad (x_1, x_2, x_3) \in \Omega \subset R^3 \tag{1}$$

supplemented with the initial condition

$$t = 0: \quad T = T_0(x_1, x_2, x_3) \tag{2}$$

boundary conditions on the reactive particle surface $\Gamma_1 \subset \partial\Omega$

$$(x_1, x_2, x_3) \in \Gamma_1: \quad \lambda_s \frac{\partial T}{\partial n} = Q_{\text{chem}} - Q_{\text{conv}} - Q_{\text{phase}} \tag{3}$$

and symmetry condition on the internal surface $\Gamma_2 \subset \partial\Omega$

$$(x_1, x_2, x_3) \in \Gamma_2: \quad \frac{\partial T}{\partial n} = 0 \tag{4}$$

To complete the statement of the problem one has to specify source terms in Eq. (3) as well as the metal oxidation kinetics. The latter is usually taken in the form of an additional differential equation

$$\frac{dh}{dt} = \phi(h, T) \tag{5}$$

with the corresponding initial condition. In Eqs. (1)–(5), t is time, $T = T(x_1, x_2, x_3, t)$ is the particle temperature, $h = h(t)$ is the oxide film thickness, $\Delta \equiv \partial^2/\partial x_1^2 + \partial^2/\partial x_2^2 + \partial^2/\partial x_3^2$ is the Laplace operator, $\partial\Omega$ is the boundary of region Ω, ∂n is the element of the normal vector to the particle surface, c is the specific heat, λ is the thermal conductivity, ϕ is a function, and indices s and 0 relate to particle material and initial conditions, respectively. Equation (3) includes source terms corresponding to heat fluxes between the particle and ambient medium due to convective heat transfer, Q_{conv}, heterogeneous chemical reaction, Q_{chem}, and phase transition, Q_{phase}. The generalized model of Eqs. (1)–(5) can be simplified in some particular cases.

1.2.2 Point model of particle ignition without metal vaporization

Assume that a solid particle is spherical and the temperature field in it is uniform. For the sake of definiteness, consider a Mg particle. Then, averaging Eqs. (1)–(4) over the particle volume, one obtains the following heat balance equation:

$$\frac{4}{3}\pi r_s^3 c_s \rho_s \frac{dT}{dt} = 4\pi r_s^2 q \rho_{\text{ox}} \frac{dh}{dt} - 4\pi r_s^2 \frac{\lambda Nu}{2r_s}(T - \tilde{T}) \tag{6}$$

The kinetic equation (5) can be taken in the form:

$$\frac{dh}{dt} = k_0 C_{\text{ox}} \psi(T) \exp(-E/RT) \tag{7}$$

In Eqs. (6) and (7), q is the chemical reaction heat related to metal oxide mass, ρ_{ox} is the metal oxide density, Nu is Nusselt number determined as $\text{Nu} = 2.0 + 0.5\,\text{Re}^{0.5}$ with the Reynolds number $\text{Re} = 2r_s U\rho/\mu$ based on the relative velocity U of gas and particle, $\tilde{T}$ is the ambient gas temperature, k_0 and E are the parameters in the empirical kinetic law for the oxide film growth, c_{ox} is the mass concentration of oxidizer, $\psi(T)$ is a function, and R is the gas constant. To take into account thermal deceleration of oxidation at high temperatures comparable with the Mg boiling temperature T_m, it is usually assumed that $\psi(T) = T_m - T$. At considerably lower temperatures, $\psi(T) = 1$.

1.2.3 Point model of particle ignition with metal vaporization

In the literature, there are some indications of the importance of metal and its oxide vaporization at the particle surface [77, 86]. Mathematical models of this phenomenon are of interest for the general theory of thermal explosion in systems with two chemical reactions exhibiting different activation energies and characteristic times [87]. The model taking into account metal vaporization follows from Eqs. (1)–(5) with a nonzero source term describing phase transition, i.e., $Q_{\text{phase}} \neq 0$. Within this model, particle temperature evolution is governed by the following equation [64]:

$$\frac{1}{3}\frac{c_s r_s}{qk}\frac{dT}{dt} = \exp(-E/RT) - c\exp(-L/RT) - \overline{\alpha}(T - \widetilde{T}) \equiv g_1(T) \qquad (8)$$

where $\overline{\alpha} = \lambda \text{Nu}/(2qr_s\rho_s k)$, $k = k_0 c_{\text{ox}}$, $c = v/k$, and L and v are the latent heat and reference rate of metal vaporization.

1.2.4 Remarks on point models

In the above models of particle ignition, a number of simplifying assumptions are adopted which are not always justified.

For metal combustion the assumption of spherically symmetric ignition process is usually adopted. However, experimental observations show that nonsymmetrical combustion modes also exist. The oxide layer possesses spherical symmetry only during the low-temperature induction phase of ignition. At high temperatures, the layer becomes nonuniform, which leads to the appearance of liquid "beads" and "caps" of oxide on the surface of the solid or liquid metal [84, 88]. It can therefore become necessary to refrain from the assumption on spherical symmetry and to include symmetry-breaking conditions when modeling combustion of metal particles. The models which are in current use are lacking in this respect.

For calculating the heat flux to particle surface the Newton law, $Q_{\text{conv}} = k_h\left(\widetilde{T} - T\right)$, is applied with T treated as the mean particle temperature. However, the Newton law is known to be valid only for steady-state heat transfer and the consequences of its application to intrinsically transient problems of particle heating and ignition are not quite clear. Moreover, the heat flux is determined by the particle surface temperature T_i rather than mean particle temperature. Thus it is assumed that the thermal conductivity of particle material is infinitely large. However this assumption can be violated when ignition of a relatively large particle of low-conductivity material is considered or when the chemical reaction rate at a particle surface is sensitive to the surface temperature. Therefore, for better representation of the generalized model of Eqs. (1)–(5), the point models have to use some correction factors for the Newton law which would allow one to take into account the transient heat transfer of metal particles with gas and nonuniform temperature distribution inside the particles.

The application of convective heat transfer correlations of the Ranz-Marshall type [89] for modeling heat fluxes between solid particles and gas under conditions of non-zero velocity slip in two-phase flows is also not fundamentally substantiated. Such correlations were derived from the measurements in steady-state flows and their use in transient two-phase flow conditions is questionable.

Regarding the overall kinetic law of particle ignition, it is usually derived by fitting the measured ignition delays and the results of calculations based on the standard particle ignition model with several unknown Arrhenius parameters (e.g., preexponential factor and activation energy). The Arrhenius parameters of the overall reaction rate constants are then found by applying the least-square procedure. In view of the above assumptions adopted in the standard model of particle heating, the Arrhenius parameters thus obtained can appear to have little common with the actual values relevant to the problem under consideration. There are many examples in the literature, when the values of preexponential factors and activation energies determined for particular conditions of particle ignition (e.g., large samples of cubic or cylindrical geometry, etc.) were applied for other conditions (fine particles of spherical or flaked shape, thin filaments, etc.). In

view of these implications, there is a need in reliable models of solid particle heating to provide the basis for improved modeling of particle ignition and combustion.

One of the promising approaches was reported by Avdeev *et al.* [90, 91] who derived the correction factors for the Newton law, which allow one to take into account the transient heat transfer of metal particles with gas and nonuniform temperature distribution inside the particles. It was implied that these correction factors can modify the conditions of particle ignition in the oxidizer gas. The dynamics of metal particle heating in a quiescent gas was calculated using three models: (1) detailed model based on the conjugate partial derivative equations of thermal conductivity in gas and particle, (2) standard point model based on the ordinary differential equation for mean particle temperature T and Newton law $Q_{\text{conv}} = k_h\left(\widetilde{T} - T\right)$, and (3) new point model, based on the ordinary differential equation for mean particle temperature T and Newton law in the form $Q_{\text{conv}} = k_{h,\text{eff}}\left(\widetilde{T} - T_i\right)$, where $k_{h,\text{eff}}$ is the effective heat transfer coefficient accounting for the transient particle heating. The approximate dependence of coefficient $k_{h,\text{eff}}$ on governing parameters and time was derived from the analytical solution for a particle with constant surface temperature. The dependence of the surface temperature on the mean particle temperature $T_i = T_i(T)$ was determined by generalizing the results of numerical calculations based on the detailed model.

Comparison of the computational results provided by the three models for Al, Mg, B, and Fe particles showed that the new model correlates much better with the detailed model than the standard model. Figures 3 and 4 show some results of calculations in terms of the mean dimensionless particle temperature T/T_0 versus dimensionless time $\text{Fo} = \kappa t / r_{s0}$ for Al and Mg particles predicted by different models.

The maximal deviations of the predicted mean particle temperature from the solution of the conjugate problem were less than 1%–2% for the new model and up to 30% for the standard point model. The largest deviations were obtained for higher gas temperatures. The latter is particularly important for the problem of metal particle ignition in oxidizer gas.

The important advantage of model [90, 91] is that it contains the particle surface temperature T_i, which may differ considerably from the mean temperature T. When solving a problem on particle ignition, the use of T_i instead of T may affect the process evolution in view of strong dependence of the rate of heterogeneous reaction on temperature.

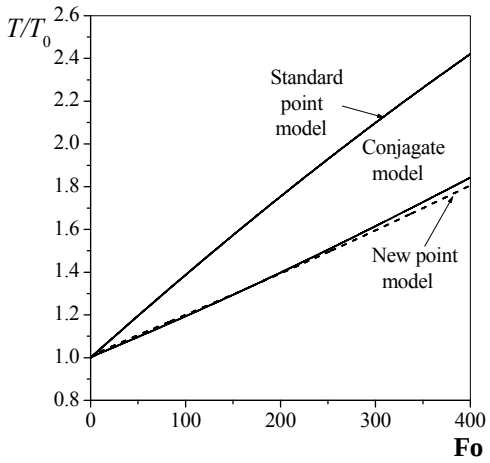

Figure 3: Predicted time histories of aluminum particle heating in air at $\widetilde{T}/T_0 = 5.46$ [90].

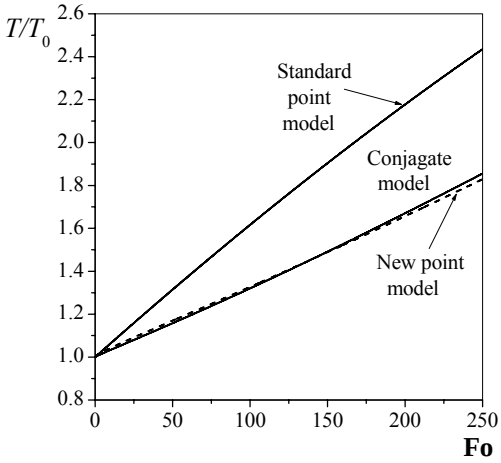

Figure 4: Predicted time history of magnesium particle heating in air at $\widetilde{T}/T_0 = 5.46$ [90].

1.2.5 Two problems in theory of particle ignition

In the following sections 1.2.6 and 1.2.7, some important issues are addressed dealing with the solution properties of the point models of Sections 1.2.2 and 1.2.3. Using the elementary theory of catastrophes, analytical and numerical methods of solving ordinary differential equations, we consider:

(1) structure of catastrophe manifolds (CM) of the point models and their correspondence to the Semenov's critical conditions in the thermal explosion theory;
(2) solvability conditions of transcendental equations for determining parameters *K* and *E*. It is implied that there can be nonuniqueness in determining *E* at a given *K*;
(3) types of particle temperature histories; and
(4) correspondence between particle ignition delay times provided by the models using the first and second approaches.

Consider a small Mg particle placed into a quiescent gaseous atmosphere at temperature $\tilde{T}$. Within the Semenov's model of thermal explosion, the equations of energy balance and oxide film growth kinetics for a particle of initial radius r_{s0} covered with the oxide film of thickness $h << r_s$ have the form of Eqs. (6) and (7) [64, 68]:

$$mc_s \frac{dT}{dt} = -Sk_h(T - \tilde{T}) + Sq\rho_{\text{ox}} \frac{dh}{dt}, \qquad \frac{dh}{dt} = Ke^{-E/RT} \tag{9}$$

where $\psi(T) = 1$ is assumed. In Eq. (9), k_h is the heat transfer coefficient, $S = 4\pi r_s^2$ is the particle surface area, $m = (4/3)\pi\rho_s r_s^3$ is the particle mass. For Mg particles, $c_s = 1100$ J/(kg·K), $\rho_s = 1740$ kg/m^3, $q = 4.9 \cdot 10^7$ J/kg, and $\rho_{\text{ox}} = 3600$ kg/m^3.

The solution of Eqs. (9) should satisfy the following initial conditions:

$$T(0) = T_0, \qquad h(0) = h_0 \tag{10}$$

Thus, the evolution of particle temperature in the gas with $\tilde{T} > T_0$ is governed by the Cauchy problem of Eqs. (9) and (10). The first of two Eqs. (9) is the autonomous ordinary differential equation. It is sufficient to analyze the zero isoclinic line and determine the types of solutions of this problem depending on some bifurcation parameters, for example, *E*, *K*, and $\tilde{T}$. In view of it, two problems should be solved.

The first problem is a direct problem formulated as follows:

Find the solution of the Cauchy problem (9) and (10), which is continuously differentiable together with its second derivative in the region $t \geq 0$.

The second problem belongs to the class of inverse problems and is formulated as follows:

Find the solution of the Cauchy problem (9) and (10) supplemented by some solvability condition with one (E) or two (E and K) unknown parameters such that one or two conditions relating these parameters are satisfied.

1.2.6 Direct problem of particle ignition without vaporization

The qualitative properties of the direct problem solution can be studied using the methods of the elementary catastrophe theory. In the dimensionless form, Eqs. (9) governing particle ignition read

$$\frac{dT}{dt} = \frac{T_{\text{ox}}}{t_1}\left(-\alpha(T - \tilde{T}) + \exp(-E/T)\right) \equiv g(T; \alpha, \tilde{T})$$

where $T_{\text{ox}} = 3\xi q/(c_s T_a)$, $\alpha = \lambda \text{Nu} T_a/(2Kr_s\rho_s\xi q)$, and $t_1 = r_s/(Kt_a)$ are some constants, T_a and t_a are the reference values of temperature and time, and $\xi = \rho_{\text{ox}}/\rho_s$. Following [92, 78, 93], consider the zero isoclinic line of the equation as a surface in the space of parameters $(T_{\text{ox}}; \alpha, t_1)$. Consider function $g(T; \alpha, \tilde{T})$ assuming that parameters α and $\tilde{T}$ are the control parameters. This enables one to construct the CM or the equilibrium surface in the $(T_{\text{ox}}; \alpha, t_1)$-space:

$$g(T; \alpha, \tilde{T}) = 0 \tag{11}$$

$$\frac{dg}{dT} = 0 \tag{12}$$

The system of Eqs. (11) and (12) then allows determination of double-degenerate critical points (DCP). If one supplements these equations by the equation

$$\frac{d^2 g}{dT^2} = 0 \tag{13}$$

and considers the solution of Eqs. (11)–(13), then this solution determines triple-degenerate critical points (TCP).

The solution of Eqs. (11)–(13) can be found explicitly:

$$X(T;\alpha,\tilde{T}) = \left(\frac{E}{2}; \frac{4}{E}e^{-2}, \frac{E}{4}\right) \equiv (T_*;\alpha_*,\tilde{T}_*)$$

The set of DCPs forms the curves of the following folds:

$$\alpha = \alpha_{\pm}(\tilde{T}) = \frac{e^{-E/T_{\pm}}}{T_{\pm} - \tilde{T}}, \quad T_{\pm}(\tilde{T}) = \frac{E}{2}\left(1 \pm \sqrt{1 - \frac{4\tilde{T}}{E}}\right) \tag{14}$$

in the plane of control parameters $(\alpha,\tilde{T})$. Note that condition $\tilde{T} = E/4$ corresponds to a cusp point, where $\alpha = \alpha_*$ and $T = T_{\pm} = T_*$. The separatrix on the plane of control parameters $(\alpha,\tilde{T})$ consists of the cusp point $(\alpha_*,\tilde{T}_*)$ and the fold curves (14). Note that DCPs of Eqs. (11) and (12) on the fold curves (14) of the catastrophe surface (11) are the solutions of Semenov equations determining the thermal equilibrium breakdown. The curves $\alpha = \alpha_-(\tilde{T},E)$ and $\alpha = \alpha_+(\tilde{T},E)$ at the $(\alpha,\tilde{T})$-plane correspond to the ignition and extinction limits, respectively.

To describe ignition of a particle with $\tilde{T} > T_0$ one has to solve the Cauchy problem (9), (10). The following analysis of qualitative features of the solution provides the information on the particle ignition criterion [61]. The ignition time is often determined in the literature as the time taken for the rate of particle temperature variation $\dot{T} = dT/dt$ or $g(T)$ to attain the maximum value.

A qualitative shape of the manifold *M* of catastrophes (ignitions) is shown in Fig. 5 in the section $\tilde{T} = const$ at $\tilde{T} < E/4$. The curves $T_i(\alpha)$ and $T_j(\alpha)$ on which the maxima and minima of function $g(T;\alpha,\tilde{T})$ are reached are also presented in Fig. 5. Curve *DC*, denoted as *I*, is a part of the zero isoclinic line of the governing equation, which is responsible for ignition. Curve *AF*, denoted as *II*, corresponds to the lower stationary particle state. Curve *DCAF* is the zero isoclinic line of the first of Eqs. (9), which is denoted as $T^0(\alpha,\tilde{T};E)$. Now, one can formulate the following Assertion.

Assertion 1. The solution of the Cauchy problem (9), (10) at $\alpha < \alpha_-(\tilde{T})$ is stabilized on part *I* of manifold *M*, and at $T_0 < T_j(\alpha)$ has two inflection points: $T_j(\alpha)$ and $T_i(\alpha)$. At $T_0 \in \left(T_j(\alpha), T_i(\alpha)\right)$, it has one inflection point. At $T_0 > T_i(\alpha)$, there are no inflection points. At $\alpha \geq \alpha_-(\tilde{T})$, the solution of the Cauchy problem is stabilized on part *II* of manifold *M* at $T_0 < T^0(\alpha,\tilde{T};E)$.

Note that in the first three cases, Assertion 1 categorizes the solutions of the Cauchy problem in terms of possible regimes of Mg particle heating with ignition. The last case corresponds to normal particle heating to some stationary state with $T^0(\alpha,\tilde{T};E) < T_-$.

The mathematical model is completely defined when the kinetic parameters in the empirical equation for the oxide film thickness are specified. In this case, it becomes possible to solve the problem numerically and determine the particle temperature history. Here, the ignition time will be treated as an instant at which the second derivative of temperature with respect to time, $\ddot{T}$, vanishes for the second time.

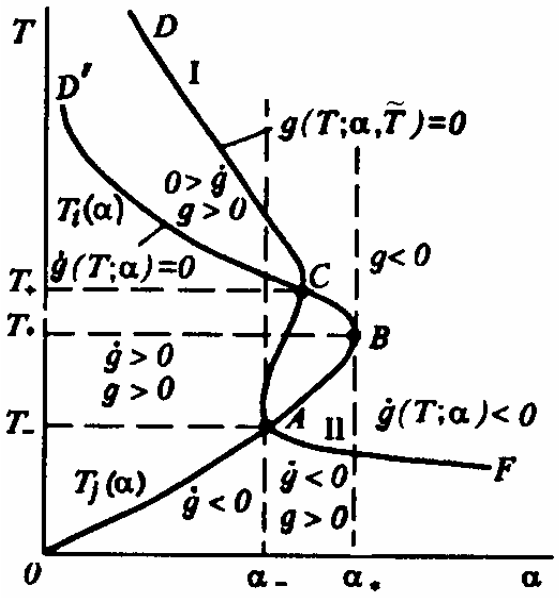

Figure 5: Qualitative shape of ignition manifold in section $\tilde{T} = const$ ($\tilde{T} < E/4$).

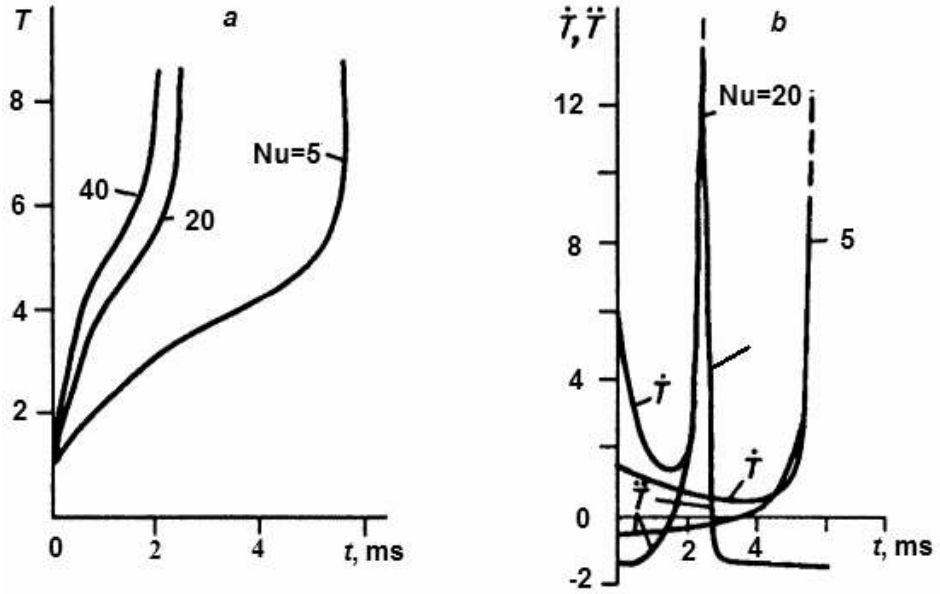

Figure 6: (*a*) Typical time histories of Mg particle temperature at $r_{s0} = 17$ μm and $\tilde{T} = 1538$ K; (*b*) time histories of first and second temperature derivatives.

Table 1: Dependence of t_{ign} on $\tilde{T}$ and Nu at $r_{s0} = 22$ μm for Mg particles.

$\tilde{T}$, K	t_{ign}, ms		
	[63]	Nu = 2	Nu = 5
1023	27	67	no ignition
1083	21	46	41
1143	17	36	24
1203	14	30	18
1263	13	26	14
1323	11	23	12

1.2.6 Direct problem of particle ignition with vaporization

In this section, the manifold of catastrophes (ignitions) for a model of thermal explosion of a Mg particle with the account for metal vaporization is analyzed. The types of particle temperature evolution in the plane of model bifurcation parameters are determined and the results obtained by different models are compared.

Within the frame of the point model, the equation governing particle temperature history has the form of Eq. (8). In order to analyze qualitatively the solution of the Cauchy problem of Eq. (8), the zero isoclinic line of this equation in the domain of variables $T, \overline{\alpha}, \widetilde{T}, c, E,$ and L is considered using the elementary catastrophe theory.

Equation (8) can be rewritten in the form:

$$\frac{dT}{d\tau} = Q^+(T) - Q^-(T) = \frac{\partial G_1}{\partial T}$$

where $Q^+(T) = e^{-2/T} - ce^{-2/\gamma T}$, $Q^-(T) = \alpha(T - \widetilde{T})$, $\gamma = E/L$, $\alpha = \overline{\alpha} T_M$, $T_M = E/(2R)$ is the reference temperature, and $G_1 = \int g_1(T)dT$ is the potential function. In a similar way as was done above, consider the conditions enabling the determination of TCPs of the potential function $G_1(T)$:

$$e^{-2/T} - ce^{-2/\gamma T} = \alpha(T - \widetilde{T})$$

$$\frac{2}{T^2} e^{-2/T} - \frac{2c}{\gamma T^2} e^{-2/\gamma T} = \alpha$$

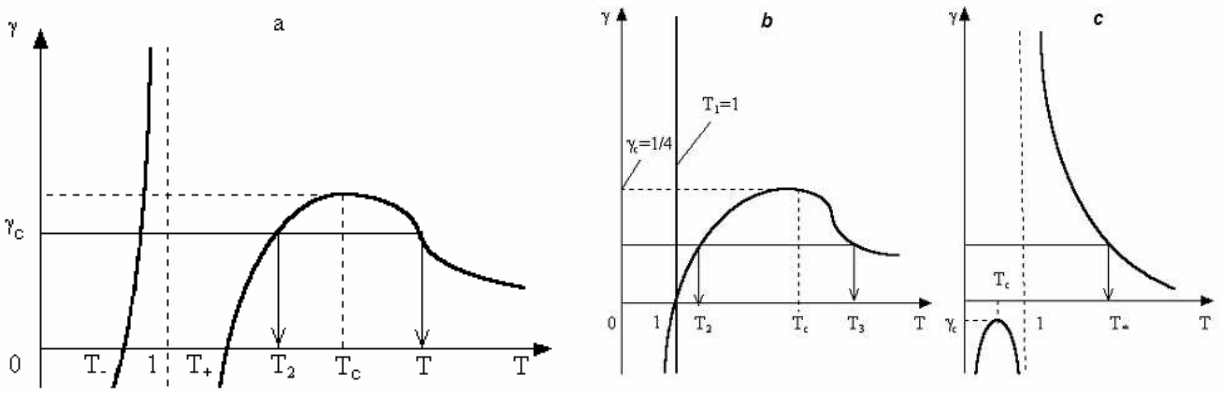

Figure 7: Diagram of zeros for determining the TCP location: (*a*) $\widetilde{T} < 0.5$, (*b*) $\widetilde{T} = 0.5$, and (*c*) $\widetilde{T} > 0.5$.

$$\left(\frac{1}{T} - 1\right) e^{-2/T} - \frac{c}{\gamma}\left(\frac{1}{\gamma T} - 1\right) e^{-2/\gamma T} = 0$$

The solution of this system of equations determining the TCP (T_*, α_*, c_*) location in parameter space (T, α, c) is equivalent to the solution of equations:

$$\gamma T^2 (T - 1) = T^2 - 2T + 2\widetilde{T}$$

or

$$P(T) \equiv \gamma T^3 - (\gamma + 1)T^2 + 2T - 2\widetilde{T} = 0 \qquad (15)$$

It is obvious that the roots of these equations depend parametrically on γ and $\widetilde{T}$. At $\widetilde{T} < 0.5$, the following representation is valid

$$\gamma = \frac{(T - T_+)(T - T_-)}{T^2(T-1)} \tag{16}$$

where $T_\pm = 1 \pm \sqrt{1 - 2\tilde{T}}$. Let us analyze qualitatively the solutions of Eq. (15) using the diagram of roots $T_* = T_*(\gamma, \tilde{T})$ shown in Fig. 7. As a result, the following Assertion can be formulated.

Assertion 2. The number and order of sequence of the roots of Eq. (15) are determined depending on γ and $\tilde{T}$ as follows:

1. $\tilde{T} < 0.5$. If
   - $0 < \gamma \le \gamma_c$, there exist three real roots $T_* = T_{1,2,3}(T_- < T_1 < 1 < T_2 < T_c < T_3)$;
   - $\gamma > \gamma_c$, there exists one real root $T_*(T_- < T_* < 1)$ and two complex conjugate roots.
2. $\tilde{T} = 0.5$. If
   - $0 < \gamma \le \gamma_c = 0.25$, there exist three real roots $T_* = T_{1,2,3}(T_1 = 1 < T_2 < T_c < T_3)$ and $T_2 = T_3$ for $\gamma = \gamma_c$;
   - $\gamma > \gamma_c$, there exist one real root $T_{*1} = 1$ and two complex conjugate roots.
3. $\tilde{T} > 0.5$: there exists one real root $T_1 > 1$ for all $\gamma > 0$.

The critical parameter here is $\gamma_c = \max \gamma(T)\big|_{T>1} = \gamma_c(\tilde{T})$ at $\tilde{T} \le 0.5$. Function $\gamma_c(\tilde{T})$ is determined parametrically: $\gamma_c = \gamma(T_c)$ as $\tilde{T} = H(T_c)$ due to equality $\left.\frac{d\gamma(T)}{dT}\right|_{T=T_c} = 0$. It can be readily shown that at realistic $\tilde{T}$ values (which do not exceed 0.2–0.3), function $\gamma_c(\tilde{T})$ is always less than unity. The proof of Assertion 2 follows from the elementary construction of function $\gamma(T)$ determined by Eq. (16) and from its continuity at $T > 1$.

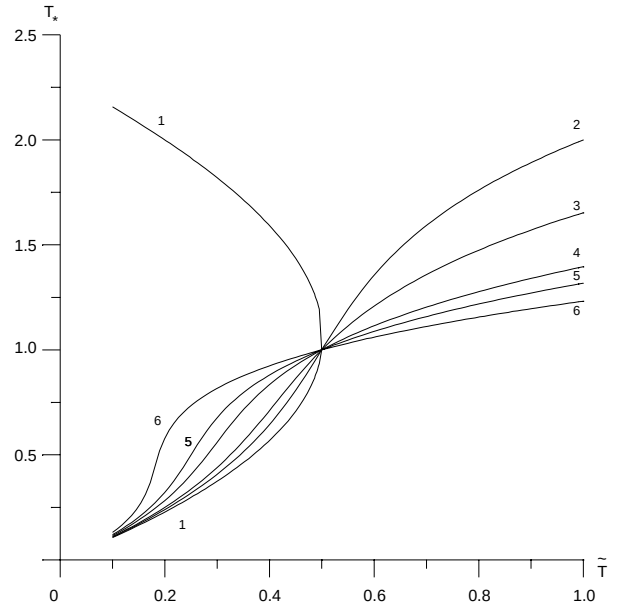

Figure 8: The diagram of roots $T_* = T_*(\tilde{T}, \gamma)$ for determining the TCP location: $\gamma = 0.1$ (1), 0.5 (2), 0.8 (3), 1.5 (4), 2.0 (5), and 3.0 (6) (in the case $\gamma = 0.1$ the branch of the third, largest root is not shown).

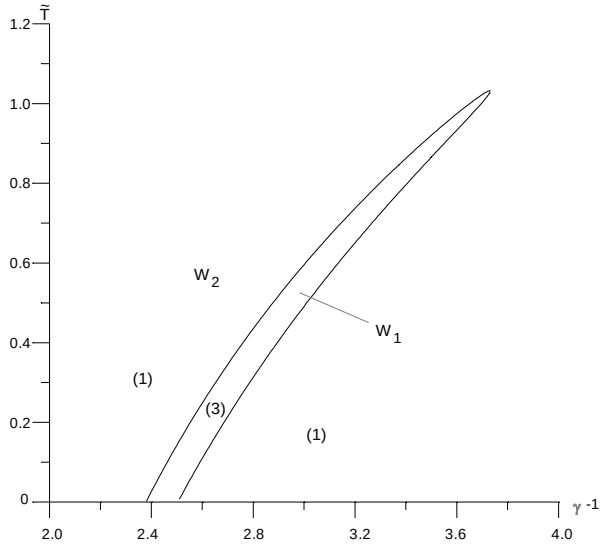

Figure 9: Partition of the parameter plane $(\gamma^{-1}, \tilde{T})$ into the regions with three (W_1) and one (W_2) TCPs; the digits in brackets show the number of TCPs.

For $\tilde{T} \le 0.5$, Eq. (15) has the following approximate solutions:

$$\text{at } \gamma << 1,\ T_{1,2} = T_{\mp} + \gamma \frac{T_{\mp}^2}{2} + \gamma^2 \frac{T_{\mp}^3}{2}\left(1 - \frac{3}{2}T_{\mp}\right) + O(\gamma^3)$$

$$T_3 = \frac{\gamma + 1}{\gamma} - (T_{*1} + T_{*2}) + O(\gamma^3) \text{ at } \gamma >> 1,$$

$$T_* = 1 + \gamma^{-1}(2\tilde{T} - 1) - 2\gamma^{-2}(2\tilde{T} - 1)^2 + O(\gamma^{-3})$$

In a general case, when γ is finite, the solution of Eq. (15) can be found numerically. The results are presented in Fig. 8 in the form of a diagram of roots $T_* = T_*(\tilde{T}, \gamma)$ for several values of γ.

Note that in practically important cases with $\gamma_c < 1 < \gamma$, the CM possesses a unique TCP similarly to the CM in the ignition model, which does not take evaporation into account. The existence of a CM with three TCPs is a new feature in the case when the activation energy of metal evaporation is much larger than that of the oxidation process, i.e., $L >> E$. This implies a possibility of nontrivial scenarios of particle ignition at a given relation between the governing parameters of the system.

Figure 9 presents the bifurcation diagram for the roots of Eq. (15) in the $(\gamma^{-1}, \tilde{T})$-plane. The diagram separates the regions of parameters with different number of TCPs and is obtained using curves $\tilde{T} = \tilde{T}_{1,2}(\gamma)$ along which the discriminator of the given cubic equation vanishes. Region W_1 is a set with three TCPs, and region W_2 is a set with one TCP. As a matter of fact, Fig. 9 is the Semenov diagram with the curves of total heat supply $Q^+(T)$ and heat removal $Q^-(T)$. Equation $Q^+(T) = 0$ possesses the following roots:

$$T = 0 \quad \text{and} \qquad T = T^0 = \frac{2(\gamma - 1)}{\gamma \ln(c^{-1})}$$

where T^0 has the meaning of stationary adiabatic temperature in the system (the temperature up to which the particle is heated in a thermally insulated volume with temperature $\tilde{T}$). It is obvious that depending on the sign of T^0 and the relation between $\tilde{T}$ and T^0, different sorts of tangency of curves $Q^+(T)$ and $Q^-(T)$ can exist (we restrict ourselves with the condition $c < 1$). The analysis of the results can be summarized in the following assertion.

Assertion 3.

1. $T^0 > 0$. Then:

1.1) if $\tilde{T} < T^0$, there exists one point of tangency (T_K, α_K), and

- at $\alpha < \alpha_K$, there exist three equilibrium positions: $(0, \tilde{T})$, (T^0, T_K), and (T_K, ∞);
- at $\alpha > \alpha_K$, there exists one equilibrium position: $(0, \tilde{T})$;

1.2) if $\tilde{T} > T^0$, there exist three points of tangency $(T_{Ki}, \alpha_{Ki}), i = 1,2,3$ numbered in the order of increasing α_K, and

- at $\alpha < \alpha_{K1}$, there exist three equilibrium positions: $(0, T_{K1})$, (T_{K1}, T^0), and (T_{K3}, ∞);
- at $\alpha_{K1} < \alpha < \alpha_{K2}$, there exists one equilibrium position lying at (T_{K3}, ∞);
- at $\alpha_{K2} < \alpha < \alpha_{K3}$, there exist three equilibrium positions: $(\tilde{T}, T_{K2})$, (T_{K2}, T_{K3}), and (T_{K3}, ∞);
- at $\alpha > \alpha_{K3}$, there exists one equilibrium position: $(\tilde{T}, T_{K2})$;

2. $T^0 < 0$. There exist two points of tangency $(T_{Ki}, \alpha_{Ki}), i = 1,2$ and

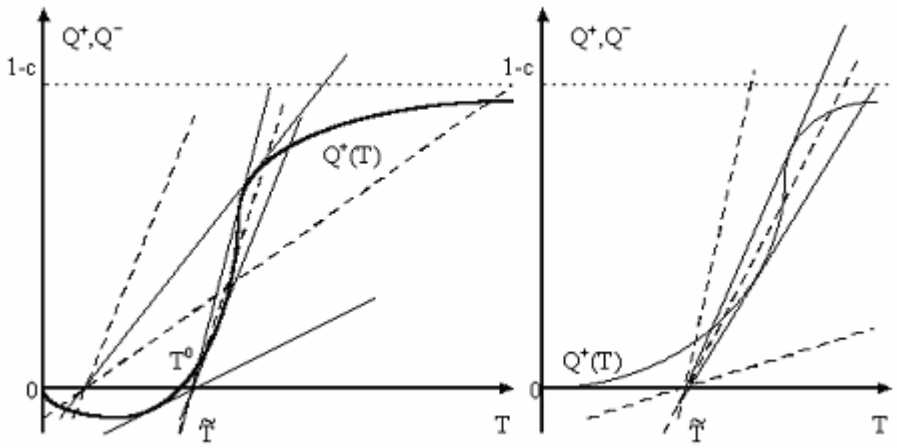

(*a*) (*b*)

Figure 10: Shapes of Semenov diagrams depending on the stationary adiabatic temperature T^0 (at $c<1$): (*a*) $T^0 > 0$, (*b*) $T^0 < 0$; dashed curves show different locations of heat removal curve $Q^-(T)$, solid curves show the limiting (tangent) locations of this curve.

- at $\alpha < \alpha_{K1}$, there exists a single equilibrium position: (T_{K2},∞);
- at $\alpha_{K1} < \alpha < \alpha_{K2}$, there exist three equilibrium positions: $(\tilde{T},T_{K1})$, (T_{K1},T_{K2}), and (T_{K2},∞);
- at $\alpha > \alpha_{K2}$, there exists a single equilibrium position: $(\tilde{T},T_{K1})$.

The proof of Assertion 3 can be readily seen from curves $Q^{\pm}(T)$ in Figs. 10*a* and 10*b*.

Some important properties of source function $Q^+(T)$ are listed below:

1) $Q^+(T) \to 0$ as $T \to 0$;

2) $Q^+(T) \to (1-c)$ as $T \to \infty$;

3) if (*a*) $0<c<1$, $\gamma>1$ or (*c*) $c>1$, $\gamma<1$, then $T^0>0$; if (*b*) $0<c<1$, $\gamma<1$ or (*d*) $c>1$, $\gamma>1$, then $T^0<0$.

Turn now to the analysis of particle temperature evolution. For this purpose, consider the typical sections $c=const$ of the CM specified by equation $Q^+(T)-Q^-(T)=0$. Upon determining the TCP coordinates one can construct the images of the fold curves in the (α,c)-plane. They are the projections of the corresponding DCPs onto the equilibrium surfaces (CMs) in the (T,α,c)-space. Using the properties of function $Q^+(T)$ and the estimates for $T_{\pm}$, one can construct a qualitative shape of the CM in sections $c=const$ as shown in Fig. 11, where typical regions in the phase plane (T,α) are determined. One can observe, for example, the following variants of temperature histories:

- at $(\alpha,T_0)\in D_1'$, a regime with explosion-free particle heating with tending to equilibrium along the lower branch $T_I'(\alpha)<\tilde{T}$;
- at $(\alpha,T_0)\in D_2'$, an ignition regime with temperature passage to the upper stable branch $T_{III}'(\alpha)$ of stationary states; and
- at $(\alpha,T_0)\in D_3'$, a regime of extinction with temperature stabilization on the branch $T_I'(\alpha)$.

The remaining variants can be analyzed in a similar way.

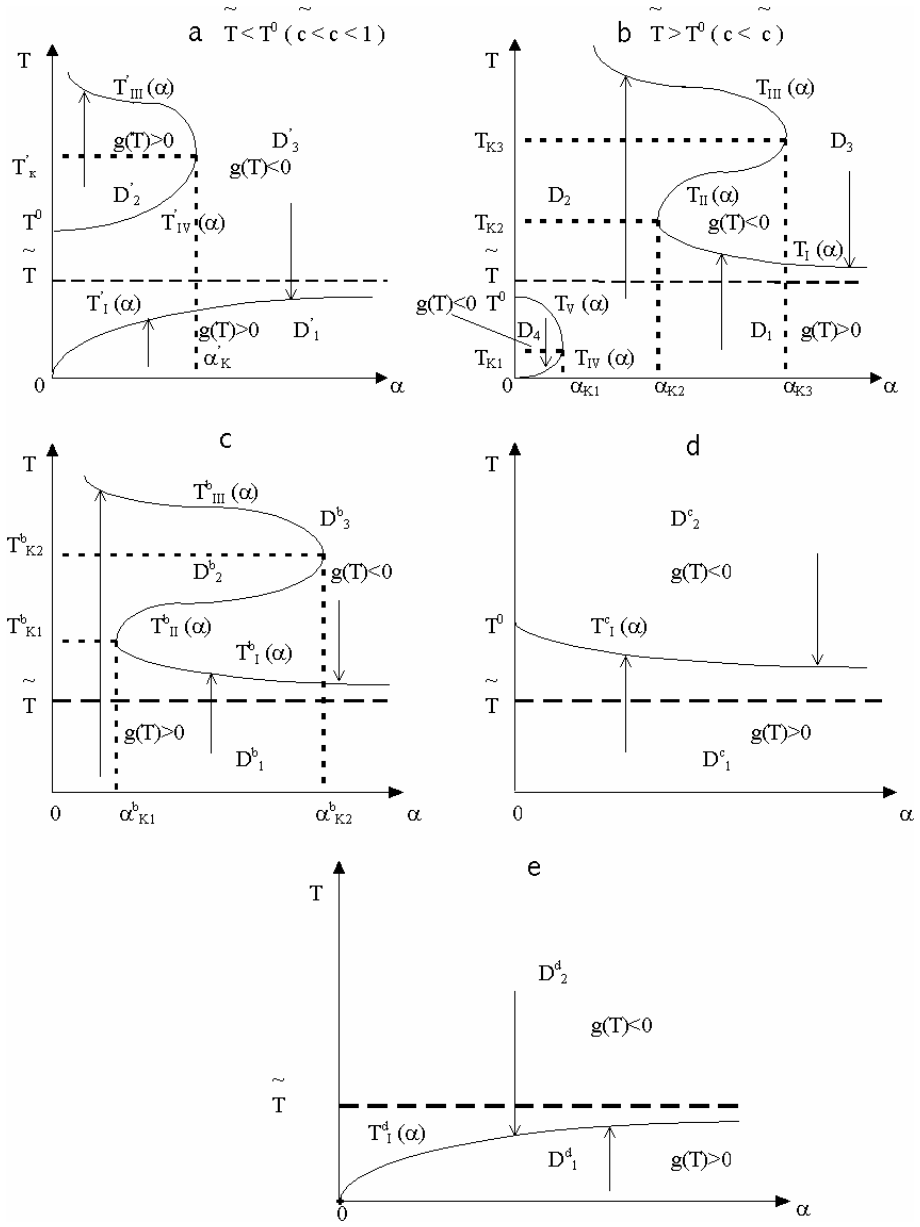

Figure 11: Structure of the ignitions manifold (typical sections $c = const$): (*a*) and (*b*) $0 < c < 1$, $\gamma > 1$; (*c*) $0 < c < 1$, $\gamma < 1$; (*d*) $c > 1$, $\gamma < 1$; (*e*) $c > 1$, $\gamma > 1$; arrows indicate possible variants of particle heating/cooling.

1.2.7 Inverse problem of particle ignition

The conducted analysis of the manifold of catastrophes (ignitions) makes it possible to categorize kinetic laws of metal particle oxidation in air with regard for metal vaporization. The equations governing the preignition state of a Mg particle can be written in the form

$$ke^{-E'/T} - ve^{-L'/T} = \alpha_0(T - \tilde{T}), \qquad k\frac{E'}{T^2}e^{-E'/T} - v\frac{L'}{T^2}e^{-L'/T} = \alpha_0 \tag{17}$$

where $\alpha_0 = \lambda \mathrm{Nu}/(2r_s\rho_s q)$, E' and L' are the activation energy and evaporation heat normalized by RT_M, and $T_M = 300$ K is the reference temperature. Following the data of [27], L'=53.333. Then Eq. (17) can be written for two arbitrary points $(r_{sj}, \tilde{T}_j)$, $j = 1,2$ at the experimental curve describing the dependence of the limiting ignition temperature in air on the particle radius [60]. This allows one to come to a closed system of transcendental equations for determining the unknown quantities E' and k (if they exist) as well as particle temperatures at the ignition limit. In so doing, the following values of kinetic parameters were derived for $v = 0.15$ m/s: E'=40.315

($E/R = 12094$ K), $k = 0.169$ m/s for fine particles (with the radius ranging from 15 to 60 μm) and $E' = 96.452$ ($E/R = 28936$ K), $k = 6.855 \cdot 10^5$ m/s for large particles (with the radius ranging from 300 to 600 μm).

It is interesting to compare the ignition delay times obtained based on these kinetic parameters and on the model without metal vaporization taken into account. As is seen from Table 2, the differences are insignificant for fine particles. For large particles, the difference does not exceed 11%.

Table 2: Comparison of ignition delay times of a Mg particle (in ms) at $\widetilde{T} = 1538$ K predicted by two models

Particle radius, μm	15	22	30	60	300	400	500	600
Model (1.2.2)	22.0	39.6	64.0	200.0	2200	3800	6000	8500
Model (1.2.3)	22.0	39.2	64.1	202.3	1990	3460	5320	7560

1.2.8 Specific features of aluminum particle ignition

Ignition of aluminum particles differs qualitatively from that of magnesium particles. At normal atmospheric conditions, aluminum particles are known to be covered by an oxide film possessing protective properties which complicate oxygen diffusion to the pure metal. Therefore the rate of high-temperature oxidation of aluminum particles depends significantly on the oxide film thickness.

Various oxidation laws of aluminum particles have been observed experimentally. In [94, 95], the growth of the oxide film was described by the exponential law

$$\frac{dh}{dt} = KC_{\text{ox}}^{n_{\text{ox}}} \exp\left(-\frac{E}{RT}\right) \exp\left(-\frac{h}{h_0}\right)$$

where C_{ox} is the oxidizer concentration near the particle surface and n_{ox} is the reaction order in relation to the oxidizer. Another frequently used equation of oxidation kinetics has the form

$$\frac{dh}{dt} = \frac{KC_{\text{ox}}^{n_{\text{ox}}}}{h^n} \exp\left(-\frac{E}{RT}\right)$$

The power exponent n in the last equation determines the dependence of the aluminum oxidation rate on the oxide-film thickness. The case with $n = 0$ was considered in Section 1.2 for magnesium particles.

In [96, 97], the oxidation rate of aluminum was assumed to be determined by the kinetics of the heterogeneous reaction and to be independent of the oxide-film thickness. It was implied that the heterogeneous reaction occurred only on the portion of particle surface not covered by oxide crystals. It was assumed in [97] that $n = 1$. This assumption resulted in the parabolic oxidation law, which is valid when the oxidation rate is limited by oxygen diffusion through the oxide film. Thus, the particle ignition model in [97] was based on the heat balance equation supplemented by the equation for the fraction of the particle surface free from the crystalline oxide. The parabolic equation of the oxide-film growth at aluminum particle surface was also considered in [72], where heat sinks due to particle vaporization and melting as well as radiation heat losses were taken into account in the heat balance equation. Analysis of numerical calculations allowed Medvedev *et al.* [72] to put forward a particular mechanism of aluminum particle ignition and determine the effect of various initial parameters on the ignition delay.

In the papers mentioned above, various approaches were used to determine the kinetic constants of the empirical ignition law. Among them are the methods of the elementary catastrophe theory, fitting of model predictions with the experimental dependencies of the ignition delay on the shock-wave Mach number [72], and some hueristic conditions relevant to the oxide-film melting point [98]. In most papers, the model predictions were compared with the measured ignition delays in terms of a single parameter, namely, the ambient gas temperature. However, it is well known from experiments [99–102] that the ignition delay is affected not only by the ambient gas temperature but

also by the particle size and oxidizer concentration in the ambient gas. It is therefore important to have a model capable of predicting aluminum particle ignition delay as a fuction of different governing parameters of the problem.

1.2.9 Point model of aluminum particle ignition

Consider a spherical aluminum particle of diameter d_s which is suddenly placed in a quiescent gas with temperature $\tilde{T}$ behind a reflected shock wave [103]. Thermal interaction of the particle with hot gas results in a heterogeneous reaction of low-temperature oxidation in a thin (as compared with the particle radius) layer on the particle surface. As a consequence, the mean particle temperature T increases and the particle can be ignited. The heat balance equation for the aluminum particle is taken in the form

$$mc_s \frac{dT}{dt} = -Sk_h(T - \tilde{T}) + Sq\rho_{\text{ox}} \frac{dh}{dt}$$

For the aluminum oxidation kinetics, the following parabolic law is used

$$\frac{dh}{dt} = \frac{KC_{\text{ox}}}{h} \exp\left(-\frac{E}{RT}\right)$$

The initial conditions for these equations are

$$t = 0: \quad T = T_0, h = h_0$$

where ρ_{ox} is the aluminum oxide (Al_2O_3) density. Thus, the problem of aluminum particle ignition in a quiescent oxidizing gas is reduced to determining the functions $T(t)$ and $h(t)$ in the region $[0, t_{\text{ign}}]$, where they satisfy the above equations and initial conditions.

There is still a need in determining the unknown parameters K and E. In the literature, different values of these parameters are reported. For example, E = 17 kcal/mole, $K = 1.9 \cdot 10^{-9}$ m^2/s, and n = 1 are reported in [101], while E = 20 kcal/mole, $K = 18 \cdot 10^3$ m^2/s, and n = 0 are reported in [96]. In general, one cannot expect the values of K and E to be constant in the wide range of governing parameters as the model under consideration oversimplifies the problem. Therefore, for using this simple model to explain the experimental dependencies of the ignition delay t_{ign} and the minimal temperature of the gas required for particle ignition $\tilde{T}_{\text{lim}}$ on the particle size it is worth to consider K as a function of the ambient temperature and particle radius.

The approach suggested herein is as follows. One can determine the value of the preexponential factor K for any two experimental points $(t_{\text{ign1}}, \tilde{T}_1)$ and $(t_{\text{ign2}}, \tilde{T}_2)$ reported, e.g., in [101]. Then $K(\tilde{T})$ can be approximated by

$$K(\tilde{T}) = \begin{cases} f(\tilde{T}), & \tilde{T} > \tilde{T}_* \\ 0, & \tilde{T} \le \tilde{T}_* \end{cases}$$

where $f(\tilde{T})$ is a linear function, and $\tilde{T}_*$ is some reference temperature. Physically, the reference temperature $\tilde{T}_*$ is the minimum temperature at which particle ignition is still possible. According to the above relationship, at $\tilde{T} < \tilde{T}_*$ the particle temperature grows solely due to heat transfer from the ambient gas and tends to $\tilde{T}_*$ in the limit.

The results of calculations for aluminum particle (d_s = 6 μm) ignition in oxygen are shown in Fig. 12 as curve 1 at the plot $\tilde{T}(t_{\text{ign}})$. The predictions are compared with the experimental data [101] (closed symbols in Fig. 12). Satisfactory agreement of predicted and measured results for intermediate oxygen temperatures is worth mentioning.

According to experiments [99, 100, 102], the minimal gas temperature $\tilde{T}_{\text{lim}}$ is also not constant and depends on the particle diameter d_s, oxygen concentration in the ambient gas C_{ox}, and ambient gas temperature $\tilde{T}$. To take it into account, one can represent the reference temperature $\tilde{T}_*$ as

$\widetilde{T}_* = \widetilde{T}_{\lim}(d_s, C_{ox})$. This dependence can be obtained, e.g., by approximating the experimental data of [102].

Let us study the influence of the particle diameter on the preexponential factor *K*, using the experimental dependencies of the ignition delay on the particle diameter [99, 100]. Note that the results reported in [99, 100] are close to each other. As a result of parametric calculations and comparison with the experiments, a certain value of *K* can be derived, e.g., for $\widetilde{T} = 2510$ K. Now, the preexponential factor can be finally represented as

$$K = (a\widetilde{T} + b)[\widetilde{T} - T_{\lim}(d_s, C_{ox})]$$

At $\tilde{T} = 2510$ K, the value of *K* predicted by this empirical formula is the same as obtained using experimental data of [100]. The activation energy *E* entering the governing equations of the model is taken equal to 17 kcal/mole in accordance with [104].

For solving the governing equations an implicit multistep method [105] was applied. The following values of physical variables were used in the calculations. For aluminum, $\rho = 2689\,\text{kg/m}^3$, $c_s = 1010$ J/(kgK) and ρ_{ox}=3970 kg/m^3. For oxygen, $\lambda = 2.4 \cdot 10^{-2} (\widetilde{T} / \widetilde{T}_0)^{0.75}$ J/(m s K), Nu = 2, and $q = 35.6 \cdot 10^6$ J/kg.

The results of calculations are shown in Figs. 12 and 13. Curves 1 and 2 in Fig. 12 are slightly different but still lie within the scatter of experimental data. In general, both figures indicate that the modified ignition model of aluminum particles provides satisfactory agreement with the experimental data on ignition delay as a function of particle size and ignition delay as a function of ambient gas temperature.

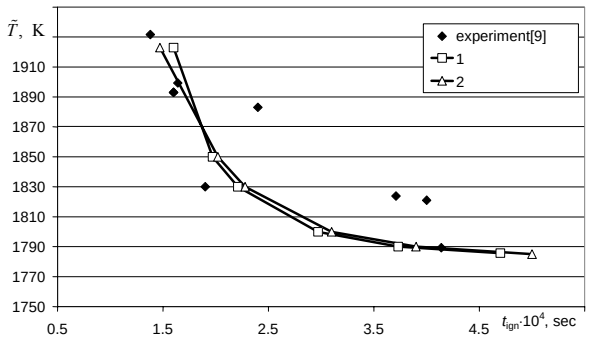

Figure 12: Measured [101] and predicted [103] dependencies of the aluminum particle (d_s = 6 μm) ignition delay on the ambient gas (oxygen) temperature. Curves 1 and 2 refer to $K = (a\widetilde{T} + b)$ and $K = (a\widetilde{T} + b)[\widetilde{T} - \widetilde{T}_{\lim}(d_s, C_{ox})]$, respectively. Closed symbols correspond to experiments [101].

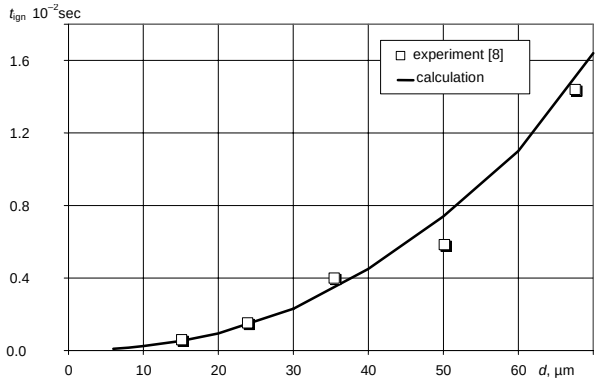

Figure 13: Measured [101] and predicted [103] dependencies of the ignition delay on the aluminum particle diameter.

1.3. Dynamic conditions

1.3.1 Ignition of metal particles behind reflected shock waves

The problem of ignition of fine metal particles in dynamic conditions behind planar incident and reflected SW was considered theoretically and experimentally in [60, 72, 74–77], and behind detonation and explosion waves in [106, 107]. It was shown in [72, 74] that the consideration of particle motion and low-temperature metal oxidation allows one to reproduce available experimental data on the dependence of ignition delay time t_{ign} on the SW Mach number M_0. To explain the experimental data on ignition of Mg particles behind reflected shock waves in a shock tube, a hypothesis on cracking of the oxide layer prior to its melting was put forward in [108, 109]. Below we provide another explanation for the effects observed in [108, 109] within the framework of a model similar to [72, 74], which takes into account particle dynamics.

Consider a gas–particle suspension of Mg particles filling the half-space bounded by a rigid wall. After a planar SW passes through it, the particles start moving and heating-up in the shock-induced flow. After the SW reflects from the rigid wall, the gas temperature increases again, while the gas velocity vanishes, i.e., $u_g = 0$. Thus, particles near the wall are subjected to variable dynamic and thermodynamic parameters of the ambient gas. Let the volume fraction of particles be sufficiently small. Then the ignition process can be described by a model similar to [72, 74]:

$$mc_s \frac{dT}{dt} = 2\pi r_s \lambda \mathrm{Nu}(\tilde{T} - T) + Sq\rho_{\text{ox}}\left[k_0 C_{\text{ox}} \exp(-E/RT) - v\exp(-L'/RT)\right] \tag{18}$$

$$m\frac{du}{dt} = \frac{1}{2} A C_D \rho U|U|$$

where u is the particle velocity, $A = \pi r_s^2$ is the particle cross-section area, $U = u_g - u$ is the relative gas–particle velocity, and C_D is the particle drag coefficient [74, 110].

The system of Eqs. (18) is supplemented with the initial data:

$$t = 0: \quad u = 0, \quad T = T_0 \tag{19}$$

which reflect the fact that the velocity and temperature of particles remain unchanged across the incident SW.

The main specific feature of problem (18), (19) is the presence of multiple stationary states at variation of a characteristic bifurcation parameter. Let us illustrate this implication of Eqs. (18), (19) for the case when particle vaporization can be neglected and particle velocity is constant. In this case, there exists a bifurcation parameter $\alpha = c_s\tau_3/(q\tau_2)$, where $\tau_3 = r_s/(3k_0 c_{\text{ox}})$ and $\tau_2 = 2c_s\rho_s r_s^2/(3\lambda\mathrm{Nu})$. The turning points of the zero curve at the (T,α)-plane were found for the following constants: $T_- = 1158$ K, $T_+ = 26960$ K, $\alpha_- = 5.946\cdot10^{-13}$, and $\alpha_+ = 1.363\cdot10^{-5}$. It turned out that at $\alpha > \alpha_-$ (e.g., $\alpha = (1+0.01)\alpha_-$), there is no ignition and particle temperature tends to its final equilibrium state. At $\alpha < \alpha_-$ (e.g., $\alpha = (1-0.01)\alpha_-$), particle ignition occurs followed by rapid temperature growth. A comparison with data of [77] for the case of zero particle velocity shows the proximity of predicted and experimental data in terms of the dependence of the ignition delay time on the particle radius.

The results of experimental studies on ignition of gas–particle mixtures of Mg powders in pure oxygen behind reflected SW were presented in [108] (particles in a shock tube were located initially at a distance of 1 cm from the end wall). For particles with diameter $d_{s0} = 2r_{s0} = 90$ μm, the values of t_{ign} are presented for different initial pressures p_0 and SW Mach numbers M_0. In Variant I, $t_{\text{ign}} = 1.4 \pm 0.1$ ms at $\mathrm{M}_0 = 4.2$ and $p_0 = 0.2$ bar; in Variant II, $t_{\text{ign}} = 2.0 \pm 0.2$ ms at $\mathrm{M}_0 = 3.9$ and $p_0 = 0.3$ bar; in Variant III, particle did not ignite at $\mathrm{M}_0 = 3.4$ and $p_0 = 0.3$ bar.

Table 3 presents the values of gas temperature behind the incident SW, $\tilde{T}$, and reflected SW, $\tilde{T}_1$, velocities D and D_1 of the waves, and gas velocity behind the incident SW for the above

Table 3: Results of experiments and computations for a monodisperse mixture.

Variant	M_0	p_0, bar	$\tilde{T}$, K	$\tilde{T}_1$, K	D, m/s	D_1, m/s	u_g, m/s	t_{ign}, ms	
								Experiment	Computation
I	4.2	0.2	1265	2470	1351	484.5	1071	1.4 ± 0.1	0.65 (1.3)
II	3.9	0.3	1129	2162	1255	457.6	984.6	2 ± 0.2	1 (2.1)
III	3.4	0.3	924.8	1698	1094	414.4	839.3	—	—

Remark. There is no ignition in Variant III. The values in brackets are t_{ign} values at refined parameters behind the SW.

Table 4: Results of experiments and computations for the polydisperse mixture.

Run	d_{s0}, μm	Experiment		Comp. run (1)		Comp. run (2)	
		$\tilde{T}_1$, K	t_{ign}, ms	t_{ign}, ms	d_{s0}, μm	t_{ign}, ms	d_{s0}, μm
1	1–40	2173	0.06	0.04	20	0.014	4
				0.12	40	0.070	20
						0.210	40
2		1470	0.11	0.065	20	0.030	4
				0.19	40	0.150	20
						0.480	40
3	63–100	2325	0.26	0.23	70	0.300	60
				0.44	100	0.600	80
						0.800	100
4		1515	0.6	0.47	70	0.900	60
				0.90	100	1.500	80
						2.100	100

values of M_0 and p_0. The numerical results are obtained using two models (see below) and presented for each of Variants I to III. Without consideration of particle velocity variation, no ignition was observed in the calculations in all three variants and particle temperature attained its stationary value. The model accounting for particle motion yields the following results: $t_{ign} = 0.65$ and 1.0 ms in Variants I and II, respectively, while in Variant III there was no ignition.

In [108], the experimental data on ignition delay times for polydisperse Mg powders were also presented. We have performed numerical calculations of the ignition delay time for each of the Variants for some selected values of particle diameters. The results are presented in Table 4 (run 1). The chosen values of a characteristic particle diameter in a polydisperse gas–particle mixture can be seen to yield the upper and lower limits for t_{ign}. The following values of thermophysical parameters were used: $\mu = 2 \cdot 10^5$ kg/(m·s) and $c_s = 1.2 \cdot 10^3$ J/(kg·K) (run 1). However, in view of elevated temperatures and pressures behind incident and reflected SW, there is a need to correct these values. The computations of the ignition delay time with corrected thermophysical data are presented in Table 4 (run 2) and in Table 3 (numbers in brackets). The thermo-physical data for high-pressure and high-temperature conditions used for the computations in Tables 3 and 4 were taken from [111]. It turns out that taking the dependence of thermophysical parameters on pressure and temperature into account leads to a better agreement between measured and calculated data.

Thus, the above analyses indicate that the results of physical experiments of [108] on ignition of Mg particles behind reflected SW in the vicinity to the shock-tube end wall are described satisfactorily by the model accounting for particle motion, low-temperature metal oxidation, and dependence of thermophysical properties of the system on temperature and pressure and do not require new mechanisms for their explanation.

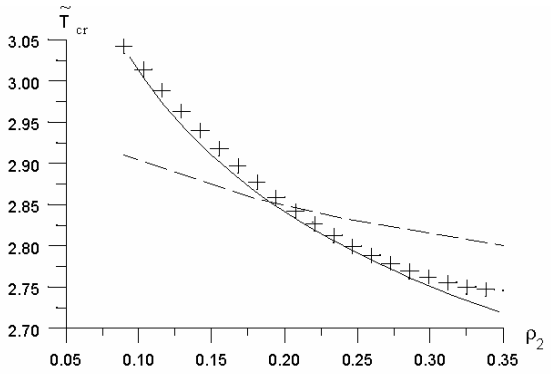

Figure 14: The minimal air temperature $\tilde{T}_{\lim}$ required for magnesium particle cloud ignition as a function of cloud density. Particle radius is 5 μm; symbols + denote experimental data of Matsko *et al.* [113]; the dashed curve corresponds to the calculation with the reaction rate constants derived for oxidation of single magnesium particle in air; the solid curve corresponds to the calculations of magnesium particle cloud ignition by Fedorov [112].

The effect of dense particle cloud on the particle ignition behavior was studied theoretically by Fedorov [112] on the example of magnesium particle cloud in air. The model included a heterogeneous chemical reaction on the particle surface and was validated against the experimental data on the minimal air temperature required for particle ignition as a function of particle radius. The predicted results are compared with the experimental data in Fig. 14.

1.3.2 Ignition of metal particles behind incident shock waves

Consider now the approaches to mathematical modeling of metal particle ignition in a high-temperature flow behind incident SW. A review of early theoretical and experimental results on particle ignition in steady-state and dynamic conditions is presented elsewhere [87]. Subsequent bibliographic references are presented in [36, 54, 112, 114–120]. They provide entire hierarchy of mathematical models of ignition waves in reacting particle suspensions in one- and two-velocity approximations. In the following, two-phase flows with very small concentrations of solid particles are considered. Description of ignition phenomena at finite particle concentrations, when it is necessary to invoke the theory of interpenetrating continua, can be found in the papers cited above.

In the region behind the propagating SW, particles accelerate up to the flow velocity and heat up due to heat exchange with the postshock gas and due to oxidation reaction. At a very small particle volume fraction, one can neglect interaction between particles and the influence of particles on the gas flow. It is implied that chemical reaction of high-temperature metal oxidation may be activated in the suspension by an incident SW. The approximation of "isolated spherical particles" [110] is therefore can be adopted. Ignition kinetics (the kinetics of high-temperature oxidation) is assumed to follow the Arrhenius law depending on the oxide film thickness with particle radius variation neglected.

The equations governing the flow of such a mixture can be written as

$$mc_s \frac{dT}{dt} = Q_{\text{chem}} - Q_{\text{conv}} - Q_{\text{phase}} - Q_{\text{rad}} - Q_{\text{int}} \tag{20}$$

$$m\frac{du}{dt} = -F_S - F_m - F_B$$

The source terms in the first Eq. (20) correspond to the heat fluxes due to:
heterogeneous chemical reaction:

$$Q_{\text{chem}} = Sq\rho_{\text{ox}} \frac{dh}{dt}$$

convective heat transfer between particle and gas:

$$Q_{\text{conv}} = S\lambda \text{Nu}(T - \tilde{T})$$

particle vaporization:

$$Q_{\text{phase}} = \frac{\lambda}{\rho c_p}\frac{S}{\text{Le}}\left(\frac{p_*}{p}\right)\exp\left(-\frac{L}{RT}\right)$$

radiation heat loss:

$$Q_{\text{rad}} = S\varepsilon\sigma(T^4 - \tilde{T}^4)$$

and particle heating and melting

$$Q_{\text{int}} = 4\pi r_s \lambda_s (T - T_0)\exp\left(-\frac{t}{t_h}\right)$$

The source terms in the second Eq. (20) correspond to the forces acting on the particle: Stokes force

$$F_s = AC_D\rho\frac{(u-u_g)|u-u_g|}{2}$$

force of virtual masses

$$F_m = -\frac{2}{3}\pi r_s^3 \rho\frac{du}{dt}$$

and Basset force

$$F_B = -6r_s^2\sqrt{\pi\rho\mu}\int_0^t (t-\tau)^{-0.5}\frac{du}{d\tau}d\tau$$

where Le is the Lewis number, c_p is the constant-pressure specific heat of gas, p_* is the reference pressure, ε is the particle blackness rate, σ is the Stefan–Boltzmann constant; $t_h = r_s^2/3a_s$ is the characteristic time of particle heating, and a_s is the thermal diffusivity of solid.

The following ignition kinetics is specified:

$$\frac{dh}{dt} = K_n c_{\text{ox}}^n h^{-n}\exp\left(-\frac{E}{RT}\right) \tag{21}$$

where K_n is the pre-exponential factor and n is the reaction order with respect to the oxidizer: $n = 1$ for Al and 0 for Mg. The system of Eqs. (20), (21) with supplementary relationships is closed with respect to the functions sought for.

The parameters characterizing the gas flow can be readily found from standard relationships for the flow behind a SW propagating at velocity D. Equations (20) and (21) written in the frame of reference moving with the SW at velocity D must satisfy the following Cauchy conditions:

$$t = t_0: \quad u = D, \quad T = T_0, \quad h = h_0 \tag{22}$$

Upon determining functions $u(x,t)$, $T(x,t)$, and $h(x,t)$, where x is the coordinate, one can find the mean density of the dispersed phase, $\rho_s(x,t)$, from the equation of dispersed-phase mass conservation. Thus, the problem of particle ignition in the shock-induced gas flow can be formulated as follows:

Find functions $u(x,t)$, $T(x,t)$, and $h(x,t) \in C^1(0,t_{\text{ign}})$ *satisfying Eqs. (20) and (21) in the region* $[0,t_{\text{ign}})$ *and the Cauchy data (22).*

The problem formulated above was solved numerically by the Gear's method. The calculations were performed for ignition of Mg and Al particles in a SW propagating in gaseous oxygen. In the calculations, the particle size was varied from 1 to 100 μm, the initial pressure was varied from 0.01 to 1 bar, and the SW Mach number was varied from 1.1 to 6.0.

The predicted results are shown in Fig. 15 as the dependence of the relative particle–gas velocity, $U = u - u_g$, in the postshock flow on time. Both experiment and calculation were made for

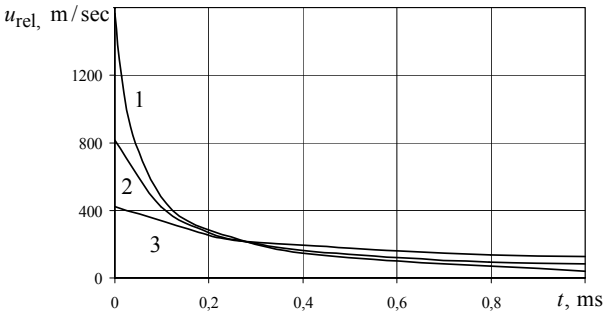

Figure 15: The temporal dependence of the particle slip velocity.

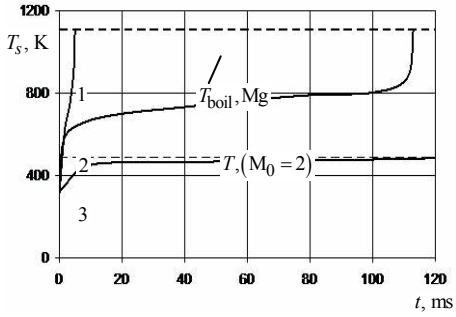

Figure 16: Predicted temperature curves for Mg particles.

$p_0 = 0.135$ bar and $M_0 = 5.0$. In the experiments, ignition of a cloud of particles with a mean diameter of 17 μm was studied. Calculations show that an increase in the SW Mach number leads to a reduction of the velocity relaxation zone length. This can be attributed to an increase in the gas density, and hence the drag force. Note that similar calculations without consideration of the Basset force result in the relaxation zone duration shorter by a factor of about 3. Note also that the effect of the force of virtual masses, F_m, is negligible as $\rho / \rho_s << 1$.

Analysis of the calculations enables one to find the conditions of and mechanisms relevant to particle ignition. It turned out that Mg particles ignite at $M_0 \in$ (2.5, 2.75) depending on the particle size. The predicted time histories of particle temperature $T = T(t)$ are presented in Fig. 16 to illustrate the effect of M_0 at $d_{s0} = 100$ μm and $p_0 = 1$ bar. In dynamic conditions, the limiting medium temperature $\widetilde{T}_{cr}$, at which ignition is still possible, is much lower than in the static conditions. Thus, for Mg particles with $d_{s0} = 100$ μm, $\widetilde{T}_{cr}$ = 640–710 K behind the incident SW, while $\widetilde{T}_{cr}$ = 920 K in static conditions. This difference is explained by an increase in the heat flux to the particle due to higher values of heat transfer coefficient between gas and particle.

It was found that at $M_0 < 4.5$ Mg particles ignite according to the thermal explosion mechanism, while at $M_0 > 4.5$ they ignite as a result of fragmentation. The corresponding ignition criteria are the conditions $T \geq T_{mel}$, where T_{mel} is the particle melting temperature, and $We > We_{cr}$, where We is the Weber number ($We_{cr} \approx 12$ is the critical Weber number at which fragmentation starts). In the calculations, the ignition delay time is taken as the least of the times of fragmentation and ignition by the thermal mechanism. The ignition due to the thermal mechanism was not found under the specified conditions. Note that "thermal explosion" was observed in computations after the particle reached a temperature less than the Mg melting temperature. Besides comparison of the flow dynamic parameter u, the predicted and measured data of [27] were compared in terms of the dependence of ignition delay time t_{ign} on the postshock temperature. The latter is shown in Fig. 17. Using the obtained kinetic constants, the computations were carried out, which allow one to extend the approximation of [27] for the ignition delay time for Mg particles of different sizes:

$$t_{ign} = A\left(\frac{d_{s0}}{17}\right)^m p_0^n \exp\left(\frac{E_*}{RT}\right)$$

where $A = 1.203 \cdot 10^4$ m·s/(bar)^n, $n = -0.866$, $m = 1.7$, and $E_* = 6.4 \cdot 10^7$ J/kmol. Similar calculations with Al particles showed that Al particles ignite following the thermal ignition mechanism (Fig. 18). The predicted value of t_{ign} for Al particles in dynamic conditions proved to be much less than in static conditions. Aluminum particles with $d_{s0} \leq 100$ μm ignite in incident SW with Mach number exceeding $M_0 > 3.2$–3.7 (depending on the particles size).

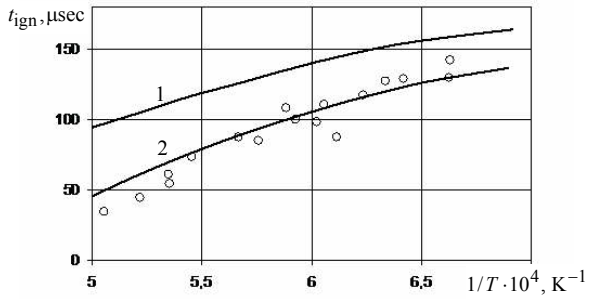

Figure 17: Comparison of measured (symbols) and predicted (solid curves) data on the dependence of ignition delay time of Mg particles on the temperature behind the incident SW.

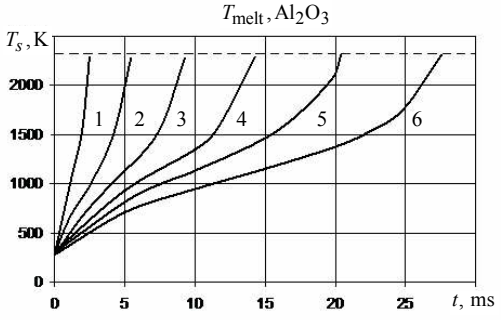

Figure 18: Computed temperature curves for the Al particle.

2. Ignition of liquid drops

Single liquid drop and spray behavior behind incident SW differs considerably from single solid particle and particle suspension behavior. It is commonly accepted that hydrocarbon drop ignition occurs in the vapor phase. Therefore a considerable increase in the specific surface area of drops caused by their aerodynamic deformation and fragmentation in the shock-induced gas flow is considered as one of the most important phenomena affecting interphase mass, momentum, and energy exchange rates and finally — ignition. Interaction of drops with gaseous flow is governed on the one hand by liquid properties, size and shape of drops and the spacing between drops, and on the other hand by local properties of gas flow. The situation is much complicated by the fact that the phases interact with each other dynamically and thermally. In the literature, there exist hundreds publications in which these interactions are studied both experimentally and theoretically.

Here, we analyze only those physical and chemical phenomena, which are directly relevant to drop ignition behind SWs. In particular we are interested in specific features of molecular mixing of fuel with air at the mixture formation stage and autoignition of two-phase mixture behind SW. Liquid fuels considered are low-viscosity *n*-alkanes or hydrocarbon fuels of the type of gasoline and kerosene.

2.1 Drop deformation

Drop deformation in the flow is the process, which is capable of influencing the interphase mass, momentum, and energy transfer. In theoretical models, a deformed drop is usually represented as an ellipsoid of revolution with large half-axis b and small half-axis a. The drop deformation degree, Δ, is defined as the ratio of a to radius r_s of a spherical drop of the same volume, $\Delta = a / r_s$. Note that in the course of deformation, a drop can take a shape resembling either oblate or prolate ellipsoid of revolution.

One can distinguish at least four mechanisms drop deformation can influence heat and mass transfer with the gas flow: (1) variation of the deformed drop cross-section area A, (2) variation of the total surface area of the drop, S, (3) variation of the aerodynamic drag coefficient C_D of the deformed drop, and (4) variation of the heat transfer coefficient k_h between gas and the deformed drop.

The maximal variations of cross-section area $A = \pi b^2$ and total surface area S are determined by the maximal possible deformation degree at which deformation is still reversible, i.e., there is still no drop fragmentation. According to [121, 122], the maximal drop deformation degree is $\Delta = 0.25$–0.44. Hence, the ratio of cross-section areas of the deformed and spherical drops

can attain the value of 2.25–4. The ratio of S to the surface area of the corresponding spherical drop can attain the values of 1.3–2.1.

The aerodynamic drag coefficient C_D for a deformed drop differs from that for a spherical drop. At high Reynolds numbers of relative motion of drop and gas, the coefficient C_D is approximately equal to 0.44 [123]. At such conditions, coefficient C_D for deformed drops can attain the values 1.6–2.2 [122], 1.8–3.0 [124] or 2.3 [125], i.e., considerably larger than for a spherical drop.

Heat transfer coefficient k_h also depends on the drop shape. For example, if the deformed drop is characterized by the equivalent Sauter mean diameter $d_{\text{eff}} = 6V/S$, where V is the ellipsoid volume, then for determining coefficient k_h one can use the approximate relationship [126]:

$$\text{Nu} = \frac{k_h d_{\text{eff}}}{\lambda} = 2.0 \exp\left[-2.22 \left(\frac{d_{\text{eff}}}{2b} - 1 \right) \right] \tag{23}$$

This relationship indicates that for a deformed drop with Δ =0.25–0.44 the heat transfer coefficient can exceed the value typical for the spherical particle by a factor of 3–5.4 even at zero relative velocity of gas and particle, $U = 0$.

Thus, increasing A and C_D can affect the dynamics of drop motion in the gas flow leading to faster relaxation of relative velocity U and therefore slow down of heat and mass transfer. On the contrary, increase of S and k_h lead to heat and mass transfer intensification. The net effect of drop deformation on its heating and vaporization in the gas flow depends on specific conditions.

There exist several models of drop deformation, e.g., [127–131]. In the existing models of drop ignition behind SW drop deformation is either not taken into account at all [132–137] or regarded using a simplified model, which does not reflect the features discussed above [138–141]. Note that drop deformation is a complex process including excitation of internal liquid circulations [142, 143] and drop oscillations as a whole. In the course of deformation, a drop can attain asymmetrical shapes which are far resembling the ellipsoid of revolution [144].

2.2 Single drop vaporization

In the postshock gas flow, the interfacial strain results in internal liquid circulation in the drop, and the conductive heat transfer is complemented by a convective heat transfer [3, 142–144]. Starting from certain values of liquid Reynolds number, the convective mechanism becomes dominating [3, 143]. Internal liquid circulation in the deformed drop can differ considerably from that in a spherical drop [2, 3]. In [145], a mathematical model of deformed drop heating and vaporization has been suggested.

Initially, at time $t = 0$, a spherical drop of radius r_{s0} is placed to the postshock gas flow. Due to the aerodynamic drag force the drop accelerates, deforms, heats up and vaporizes. In addition, internal liquid circulation is induced in the drop. The task is to determine the rate of drop vaporization and drop lifetime in these conditions. Assume that the drop takes the shape of ellipsoid of revolution. The properties of liquid will be denoted by index l, while the parameters at the drop surface by index i. At this step, we will restrict ourselves by considering the situations when the drop deformation does not attain the critical stage followed by drop breakup. As is known (see Section 2.3), drop breakup occurs at Weber number $\text{We} = d_{s0}\rho U_0^2/\sigma_l \geq 12$, where σ_l is the surface tension, $d_{s0} = 2r_{s0}$ is the spherical drop diameter. The critical deformation stage is attained at Δ = 0.25–0.44 or b/r_s =1.5–2.0 [130].

To determine the most important geometrical parameters of the drop — b, a, A, and S — use the deformation equation [131]:

$$\frac{d^2y}{dt^2} = \frac{C_F}{C_b}\frac{\rho}{\rho_l}\frac{U^2}{r_s^2} - \frac{C_k\sigma_l}{\rho_l r_s^3}y - \frac{C_d\mu_l}{\rho_l r_s^2}\frac{dy}{dt} \tag{24}$$

where $y = \delta/(C_b r_s)$ is the dimensionless deformation, δ is the displacement of the drop equator from the equilibrium position in the plane normal to the direction of the relative velocity U, and $C_b = 0.5$, $C_F = 0.333$, $C_k = 8$, and $C_d = 5$ are the dimensionless coefficients. The initial conditions for Eq. (24) are:

$$t = 0: \qquad y = 0; \qquad \frac{dy}{dt} = 0 \tag{25}$$

For ellipsoid of revolution, the large half-axis b is equal to $b = r_s + \delta = r_s(1 + C_b y)$. The small half-axis a can be determined from the condition of constant drop volume in the cause of deformation: $V = (4/3)\pi a b^2 = (4/3)\pi r_s^3$. Parameters A and S can then be readily determined.

The equation of heat balance for the deformed drop can be written in the form:

$$c_l m \frac{dT}{dt} = Q_{i-} \tag{26}$$

where $m = V\rho_l$ is the drop mass, Q_{i-} is the total heat flux from the drop surface to drop interior (index $i-$ means that the value of heat flux is taken at the drop surface from the liquid side). Heat flux Q_{i-} is a function of temperature and velocity fields inside the drop, i.e., $Q_{i-} = f(t, T_i, T, u_i, ...)$, where u_i is the liquid velocity at the drop surface. The heat flux Q_{i+} from the gas side (index $i+$ means that the value of the heat flux is taken at the drop surface from the gas side) for the evaporating drop is given by the relationship:

$$Q_{i+} = Q + L\frac{dm}{dt}$$

where Q is the full heat flux toward the drop from the gas phase and L is the latent heat of vaporization. Due to continuity of heat flux, $Q_{i-} = Q_{i+}$, and Eq. (26) takes the form:

$$c_l m \frac{dT}{dt} = Q + L\frac{dm}{dt} \tag{27}$$

Initial conditions for Eq. (27) are formulated as follows:

$$t = 0: \qquad T = T_0 \tag{28}$$

The heat flux Q in Eq. (27) is given by the relationship $Q = Sq_h$, where q_h is the heat flux per unit surface area of the drop. To determine q_h one can apply the Newton law $q_h = k_h(\tilde{T}_\infty - T_i)$ with ∞ denoting gas properties at a large distance from the drop surface. Note that the Newton law is applicable only to the steady-state heat transfer. Nevertheless, as shown in [146], it can be applied to problems of transient heat transfer by introducing an effective thermal conductivity of gas. In the standard drop vaporization model (e.g., [147]), it is assumed that $\lambda = \lambda(\overline{T})$, where $\overline{T} = (\tilde{T} + T_i)/2$ is some characteristic gas temperature. Heat transfer coefficient k_h in the Newton law is given by [2, 146]:

$$k_h = \frac{\mathrm{Nu}}{d_{\mathrm{eff}}}\lambda\frac{\ln(1+B)}{B} \tag{28}$$

where B is the mass transfer coefficient. In general, Nusselt number in Eq. (28) depends on the drop shape (see Eq. (23)) and Reynolds number based on the relative velocity $\mathrm{Re} = d_{\mathrm{eff}}\rho|U|/\mu$. In the absence of proper relationships for deformed drops, it is worth to utilize the corresponding dependence Nu = Nu(Re) for a spherical drop [148] as a first approximation:

$$\mathrm{Nu} = 2.0\exp\left[-2.22\left(\frac{d_{\mathrm{eff}}}{2b} - 1\right)\right] + 0.6\,\mathrm{Re}^{1/2}\,\mathrm{Pr}^{1/3} \tag{29}$$

where $\mathrm{Pr} = \mu/\rho a_T$ is the Prandtl number and a_T is the gas thermal diffusivity. Relationship (29) indicates that at high Reynolds numbers Nusselt number for a spherical drop in air can attain values up to an order of magnitude higher than Nu = 2.0.

Reynolds number Re can be determined from the solution of drop motion equation (18) with the initial condition

$$t = 0: \qquad u = u_0 \tag{30}$$

For the evaporating drop, aerodynamic drag coefficient C_D depends not only on the drop shape, but also on the mass transfer coefficient B and on the physical properties of gas and liquid, which determine the liquid velocity at the drop surface.

The effect of B on C_D is usually taken into account as [2] $C_D = C_{D,ne}/(1+B)$, where $C_{D,ne}$ is the aerodynamic drag coefficient of a nonevaporating drop (index *ne*). The effect of drop shape on the value of $C_{D,ne}$ can be taken into account using the relationship [149] $C_{D,ne} = C_{Ds,ne}(1+2.632y)$. Aerodynamic drag coefficient of a solid sphere $C_{Ds,ne}$ is equal to [150]:

$$C_{Ds,ne} = \begin{cases} \dfrac{24}{\mathrm{Re}}\left(1+0.15\,\mathrm{Re}^{0.687}\right) & \text{at } \mathrm{Re} < 10^3 \\ 0.44 & \text{at } \mathrm{Re} \geq 10^3 \end{cases}$$

Thus, at high Reynolds numbers and large drop deformations ($y \approx 1$) coefficient $C_{D,ne}$ may attain the value of 1.5 typical for a disk-shaped body. This value is larger by a factor of 3.4 than the value $C_{Ds,ne} = 0.44$ typical for a spherical body.

The effect of liquid motion on the drop surface on the value of $C_{Ds,ne}$ can be taken into account by using the results of numerical calculations [144]:

$$\frac{C'_{Ds,ne}}{C_{Ds,ne}} = \left(\frac{2+3\mu_l/\mu}{3+3\mu_l/\mu}\right)\left(1-0.03\frac{\mu}{\mu_l}\mathrm{Re}^{0.65}\right)$$

where $C'_{Ds,ne}$ is the aerodynamic drag coefficient of a spherical liquid drop. The latter relationship approximates well the analytical results at low and high Reynolds number Re, but its application is in general limited by the range of viscosity ratio μ_l/μ, studied in [144].

Mass transfer coefficient B is defined as $B = (Y_{vi} - Y_{v\infty})/(1-Y_{vi})$ [2, 146], where index v relates to the liquid vapor and Y is the mass fraction.

The rate of drop mass variation due to vaporization entering Eq. (27) is found from the equation:

$$\frac{dm}{dt} = -Sj \tag{31}$$

where $j = 2\rho D \ln(1+B)/d_{\mathrm{eff}}$ is the vapor mass flow rate per unit drop surface area [2, 146] and D is the binary diffusion coefficient for gas and vapor. The initial condition for Eq. (31) is:

$$t = 0: \quad m = m_0 \tag{32}$$

Many relationships discussed above contain, explicitly or implicitly, the drop surface temperature T_i. In particular, temperature T_i plays important role in determining heat flux Q_{i-}. For determining T_i, the following considerations will be used.

When mean drop temperature T attains the value of saturation temperature ('wet-bulb' temperature) $T_i = T_{wb}$, the heat flux to drop interior vanishes, i.e., $Q_{i-} = Q_{i+} = 0$, and entire heat flux Q is consumed for liquid vaporization. The initial period in drop evolution, when $Q_{i-} \neq 0$ or $T < T_{wb}$, is referred to as the transient heating period. The period when $Q_{i-} = Q_{i+} = 0$ or $T = T_{wb}$ is referred to as the period of quasisteady drop vaporization. In the latter case, instead of Eq. (27) one can write $T = T_i = T_{wb}$ and $Q = -v\,dm/dt$. Denote the duration of the transient heating period as t_h, duration of the quasisteady vaporization period as Δt, and the total lifetime of the drop as t_l. Then $t_l = t_h + \Delta t$.

In accordance with [145], internal liquid circulation in the drop can result in a considerable decrease of the transient heating period t_h compared with the standard case when only conductive heat transfer is taken into account. At $t \geq t_h$, internal circulation exerts no effect on the drop vaporization dynamics. This means that at $t > t_h$ the drop evaporates independently of internal convective flows. Thus, internal liquid circulation can decrease the drop lifetime no more than by the value of t_h. Note that in the standard model of spherical drop vaporization without internal circulation the duration of the transient heating period for heavy hydrocarbon drops can be rather long (up to $t_h \approx t_l$), in particular at high gas temperatures and pressures [150].

The effect of internal liquid circulation on drop heating during the transient period can be taken into account by introducing the coefficient of internal heat transfer intensification, $\theta = t_h / t_h^o \leq 1$, i.e., $Q_{i-} = \theta^{-1} Q_{i-}^o$, where upper index "o" relates to a spherical drop without internal liquid circulation. To determine coefficient θ one can use the results of numerical solution of the problem on spherical drop heating in the gas flow in the approximation of constant surface temperature $T_i = const$ [145].

To substantiate the possibility of using such an approximation, let us determine the wet-bulb temperature T_{wb}. Substituting the above relationships to the condition $Q_{i-} = 0$ gives the following algebraic equation for $T_i = T_{wb}$:

$$\mathrm{Nu}\lambda(\tilde{T}_\infty - T_i) = 2\rho D L \frac{Y_{vi} - Y_{v\infty}}{1 - Y_{vi}} \tag{33}$$

In Eq. (33), parameters λ, ρ, D, L, and Y_{vi} are the functions of temperature T_i, therefore its solution should be found by iterations. For checking the validity of Eq. (33), detailed numerical calculations of spherical drop heating and vaporization were performed using the model [150], which does not take into account relative motion of drop and gas. In the computational code [150], partial differential equations for both liquid and gas phase are solved using the approximation of multicomponent diffusion for the gas phase and variable thermophysical properties of phases. To demonstrate the predicting capability of model [150], Fig. 19 shows a comparison of predicted and measured drop surface regression curves for a *n*-heptane drop. In the simplest standard model of drop vaporization based on the quasi-steady vaporization law, the dependence $d^2(t)$ is known to be linear. In the model of [150] this dependence is more complex: due to liquid thermal expansion the $d^2(t)$ function exhibits a nonlinear behavior.

Solid and dashed curves in Fig. 20 show the predicted dynamics of surface temperature T_i and mean temperature T for *n*-dodecane drop [145]. Horizontal dash-and-dot lines correspond to the solution of Eq. (33) at Nu = 2.0. Termination of the curves in Fig. 20 corresponds to complete drop evaporation (lifetime t_l). Remind that the transient heating period duration t_h is the time taken for the mean drop temperature to attain the value of the wet-bulb temperature.

Analysis of Fig. 20, as well as the results of calculations at other values of $\tilde{T}$ and p and for other liquids (*n*-heptane, *n*-octane, methanol, etc.), result in the following conclusions:

(1) The time taken for drop surface temperature T_i to attain the value close to wet-bulb temperature T_{wb} is considerably smaller than the total drop lifetime t_l, in particular at high gas temperatures $\tilde{T}$.

(2) At high gas temperatures, the duration of the transient heating period t_h is comparable with the total drop lifetime t_l.

(3) Equation (33) provides a good estimate for the wet-bulb temperature T_{wb} in a wide range of gas temperature and pressure, as well as physical properties of liquid.

If the drop is placed in the postshock gas flow, the values of wet-bulb temperature will be somewhat different from the value relevant to drop vaporization in a quiescent atmosphere. This is evident from Eq. (33). At $\mathrm{Re} \neq 0$, Nusselt number in Eq. (33) can be estimated based on Eq. (29) for a spherical drop.

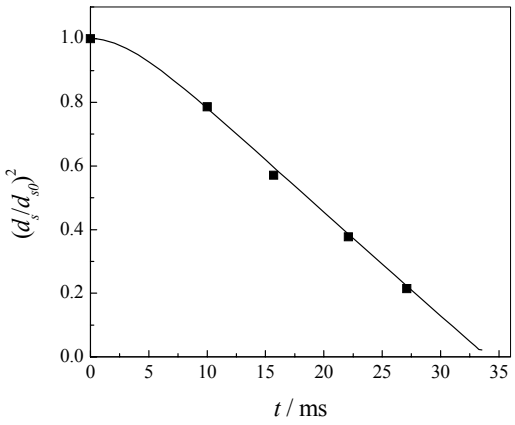

Figure 19: Comparison of predicted (curve) and measured (points) dynamics of *n*-heptane drop surface regression at vaporization in air, $d_{s0} = 70$ μm, $T_0 = 293.15$ K, $\tilde{T} = 573.15$ K [150].

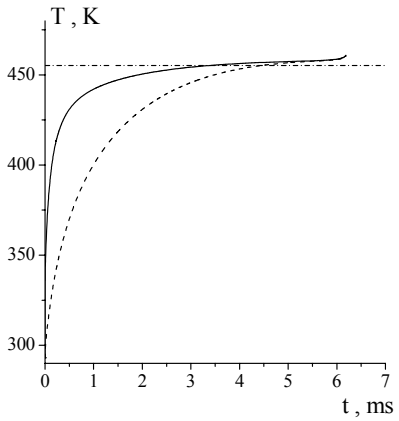

Figure 20: Predicted time histories of surface (solid curve) and mean (dashed curve) temperatures of a vaporizing *n*-dodecane drop 50 μm in diameter at T_0 = 293 K, p = 0.1 MPa, and $\tilde{T}$ = 1500 K [145]. Dash-and-dot line corresponds to wet-bulb temperature found from Eq. (33).

In order to understand, how Nusselt number affects the wet-bulb temperature, additional calculations have been made. Variation of the wet-bulb temperature with Nusselt number is most pronounced at high pressures and low gas temperatures. Nevertheless, the wet-bulb temperature for liquid drops in the gas flow can differ no more than by 30–40 K compared to the quiescent conditions with Nu = 2. Figure 21 demonstrates this implication for *n*-dodecane drops.

Thus, the results obtained allow one to adopt an important assumption that drop surface temperature T_i attains the value of T_{wb} instantaneously, i.e., $T_i = T_{wb} = const$. This assumption makes it possible to simplify considerably the modeling of drop heating, using Eq. (33) for determining the wet-bulb temperature at Nu = 2. To find the value of coefficient θ, one can use the results of [145].

Figure 22 shows the predicted dependencies of mean *n*-heptane drop temperature on the normalized time t/t_h^o at different liquid Reynolds numbers $\mathrm{Re}_l = \rho_l u_i r_s / \mu_l$ [145]. The calculations were performed using the approach of [145]. Clearly, internal circulation leads to a significant reduction of the transient heating period t_h. To generalize the results, detailed calculations of drop heating in constant and variable dynamic conditions were made. In constant dynamic conditions, the relative velocity was kept constant ($U = U_0$), whereas in variable dynamic conditions drop heating was calculated with regard for drop motion according to Eq. (18) with initial conditions (30). The following correlation for the mean coefficient θ was suggested in [145]:

$$\begin{aligned} &\theta = 1 && \text{at} \quad \mathrm{Re}_l \le \mathrm{Re}_l^* \\ &\theta = C_1 \log(\mathrm{Re}_l) + C_2 && \text{at} \quad \mathrm{Re}_l^* < \mathrm{Re}_l < \mathrm{Re}_l^{**} \\ &\theta = C_3 \log(\mathrm{Re}_l) + C_4 && \text{at} \quad \mathrm{Re}_l > \mathrm{Re}_l^{**} \end{aligned} \tag{34}$$

where Re_l^* and Re_l^{**} are some characteristic values of Reynolds number. Their values and the values of constants for *n*-heptane and *n*-dodecane drops are presented in Tables 5 and 6. Thus, Eqs. (34) allow one to account for the effect of internal liquid circulation on heat and mass transfer of spherical liquid drop with gas flow at $t < t_h$.

To model deformed drop heating, one can assume, in addition to the assumptions adopted in [145], that drop deformation is quasistatic, i.e., characteristic time required for the establishment of internal motion is small compared with the characteristic heating time of the drop. Validity of this

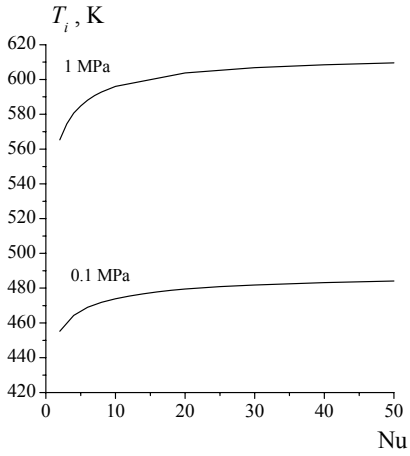

Figure 21: Predicted dependencies of wet-bulb temperature T_{wb} on Nusselt number Nu for *n*-dodecane drops at $\tilde{T}$ = 1500 K and p = 0.1 and 1 MPa [150].

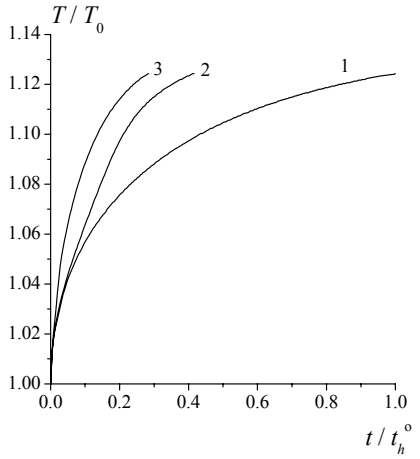

Figure 22: Predicted dependencies of mean temperature of spherical *n*-heptane drop on normalized time at $T_0 = 300$ K, $\tilde{T} = 750$ K, p = 0.1 MPa and d_{s0} = 200 μm [150]. Curve *1* corresponds to $\mathrm{Re}_l = 0$, curve *2* — to $\mathrm{Re}_l = 1.3$, curve *3* — to $\mathrm{Re}_l = 13$.

Table 5: Characteristic Reynolds numbers $\mathrm{Re}_l = \rho_l u_l r_s / \mu_l$.

Liquid	Re_l^*	Re_l^{**}
n-heptane	0.59	11.60
n-dodecane	0.19	3.74

Table 6: Coefficients in approximation relationships for θ .

Liquid	C_1	C_2	C_3	C_4
n-heptane	– 0.410	0.910	– 0.182	0.670
n-dodecane	– 0.395	0.700	– 0.193	0.600

assumption was checked by 3D numerical simulation of transient heating of deformed liquid drops. The mathematical statement of the problem for the deformed drop was similar to that for a spherical drop [143, 145] with one exception. Since the analytical solution for the internal flow filed is available only for a spherical drop, the corresponding flow fields in the ellipsoidal drops were found from the steady-state solution of Navier–Stokes equations with special boundary conditions on the drop surface.

Based on the calculated velocity fields inside the deformed drops, the equation of convective thermal conductivity was solved. As a result, a coefficient of heat transfer intensification for deformed drops θ' was derived. The calculations revealed that $\theta' \approx \theta\theta_f$, where $\theta_f = t_h^e / t_h^o$ (upper index "*e*" relates to the deformed drop without internal liquid circulation) is function of drop shape only and virtually the same for liquids with different physical properties (*n*-heptane, *n*-octane, *n*-dodecane, water and methanol) at different intensity of internal liquid circulation. The results of calculations were approximated by the second-order polynomial:

$$\theta_f = -0{,}78 + 3{,}67\Delta - 1{,}89\Delta^2 \quad \text{at } \Delta < 1 \tag{35}$$

for oblate ellipsoid of revolution and

$$\theta_f = 0{,}65 + 0{,}77\Delta - 0{,}42\Delta^2 \quad \text{at } \Delta > 1 \tag{36}$$

for prolate ellipsoid of revolution. The approximation error of Eqs. (35), (36) is less than 6%.

Coefficient θ_f^{-1} can be treated as an additional correction factor to the heat flux $\dot{Q}_{i-}$, i.e.,

$$\dot{Q}_{i-} = \dot{Q}_{i-}^{o}(\theta\theta_f)^{-1} \tag{37}$$

where coefficients θ and θ_f are given by Eqs. (34) and (35) or (36).

Differential equations (24), (27), (18), and (31) with initial conditions (25), (28), (30), and (32), as well as additional relationships presented above allow one to predict the behavior of a liquid drop in the gas flow with regard for drop deformation, motion, transient heat transfer and vaporization, and therefore to determine the drop lifetime. As compared to the standard vaporization model of a spherical drop, Eqs. (23)–(37) include at least eight supplementary factors which can affect the drop lifetime in the gas flow. These are: (*i*) internal liquid circulation which affects the duration of the transient heating period from the initial temperature T_0 to wet-bulb temperature T_{wb}, (*ii*) variation of drop surface area *S*, (*iii*) variation of heat transfer coefficient k_h due to drop deformation, (*iv*) variation of heat transfer coefficient k_h due to relative motion of drop and gas, (*v*) variation of deforming drop cross-section area *A*, (*vi*) variation of aerodynamic drag coefficient C_D due to drop vaporization, (*vii*) variation of coefficient C_D due to drop deformation and (*viii*) variation of coefficient C_D due to liquid motion at the drop surface.

All factors (*i*)–(*viii*) can be considered as corrections to a standard model. Since corrections (*i*)–(*iv*) relate to the heat balance equation and corrections (*v*)–(*viii*) relate to the drop motion equation, they can be conditionally referred to as "thermal" and "dynamic" corrections, respectively. These corrections can be readily introduced to the standard model, e.g., [147]. Below we show some examples of calculations with and without these corrections. The problem was solved by the Runge–Kutta method of the 4th order for drops of various primary hydrocarbons at different temperatures and pressures of ambient air and at different Weber numbers determining drop deformation. Thermophysical properties of liquids were treated as functions of pressure and temperature.

The results of calculations with corrections (*i*)-(*viii*) were compared with the results predicted by model [147] at $U \neq 0$ ($\mathrm{We}_0 \neq 0$). The calculations revealed that the most pronounced effect on the drop lifetime is produced by "thermal" corrections (*i*)–(*iv*), whereas "dynamic" corrections (*v*)–(*viii*) play an insignificant role.

Figure 23 shows the predicted time histories of "fine" (d_{s0} = 25 μm) *n*-dodecane drops at $\tilde{T}$ = 1000 K, T_0 = 300 K, and *p* = 1 MPa, and different Weber numbers We. Solid curves correspond

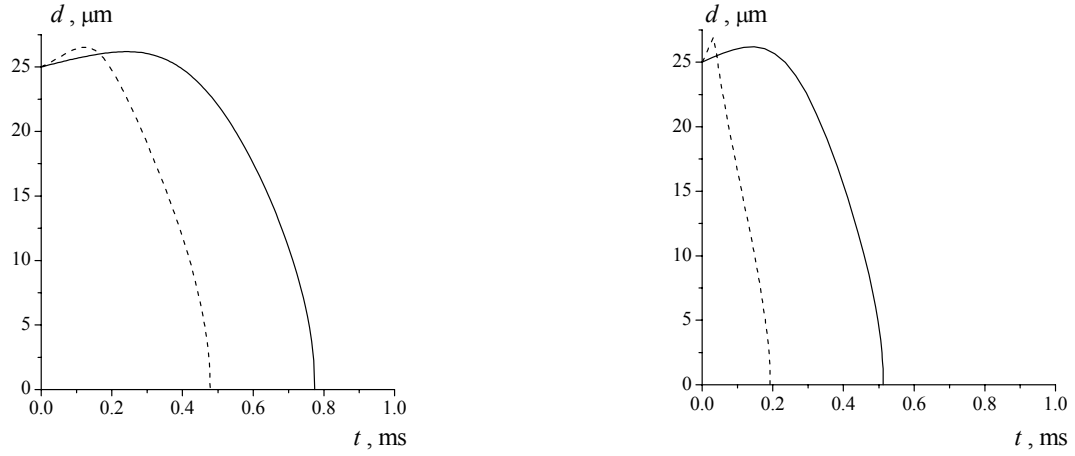

Figure 23: Time histories of *n*-dodecane drop diameter predicted by standard model (solid curves) and modified standard model with "thermal" corrections (*i*)-(*iv*) (dashed curves) at d_{s0} = 25 μm, $\tilde{T}$ = 1000 K, T_0 = 300 K and *p* = 1 MPa [145]. (*a*) We_0 = 0.2; (*b*) We_0 = 12.

to model [147] and dashed curves to the modified model [147] with "thermal" corrections (*i*)–(*iv*) [145].

Analyzing the computational results at different values of d_{s0}, $\tilde{T}$, p, and We, one comes to the following conclusions regarding the effect of "thermal" corrections (*i*)–(*iv*) on the drop lifetime:

(1) Corrections can result in a considerable reduction of drop lifetime (up to a factor of 2.5);
(2) Effect of corrections on drops of less volatile fuel is more pronounced;
(3) Effect of corrections increases with Weber number We;
(4) Effect of corrections increases with pressure p;
(5) Effect of corrections increases with gas temperature $\tilde{T}$;
(6) Variation of d_{s0} is not virtually reflected on the effect of corrections.

Less pronounced effect of "thermal" corrections on the volatile fuel drop lifetime is explained by a shorter transient heating period t_h.

2.3 Drop breakup

As follows from physical reasoning and dimensional analysis, breakup is governed by the following basic dimensionless numbers representing ratios of the forces: aerodynamic force to surface tension or Weber number $\mathrm{We} = \rho U^2 d_s / \sigma_l$, aerodynamic force to viscous force in the gas phase or Reynolds number $\mathrm{Re} = \rho |U| d_s / \mu$, and viscous force to surface tension in the liquid phase or Ohnesorge number $\mathrm{Oh} = \mu_l / (\rho_l \sigma_l d_s)^{1/2}$. Ohnesorge number comes into play when viscosity of liquid is high therefore, when breakup of such inviscid liquids as hydrocarbons for which Oh < 0.1 are considered, its effect on mass transfer can be neglected. Generally, depending on the Weber number, the breakup modes look as shown in Fig. 24 [151].

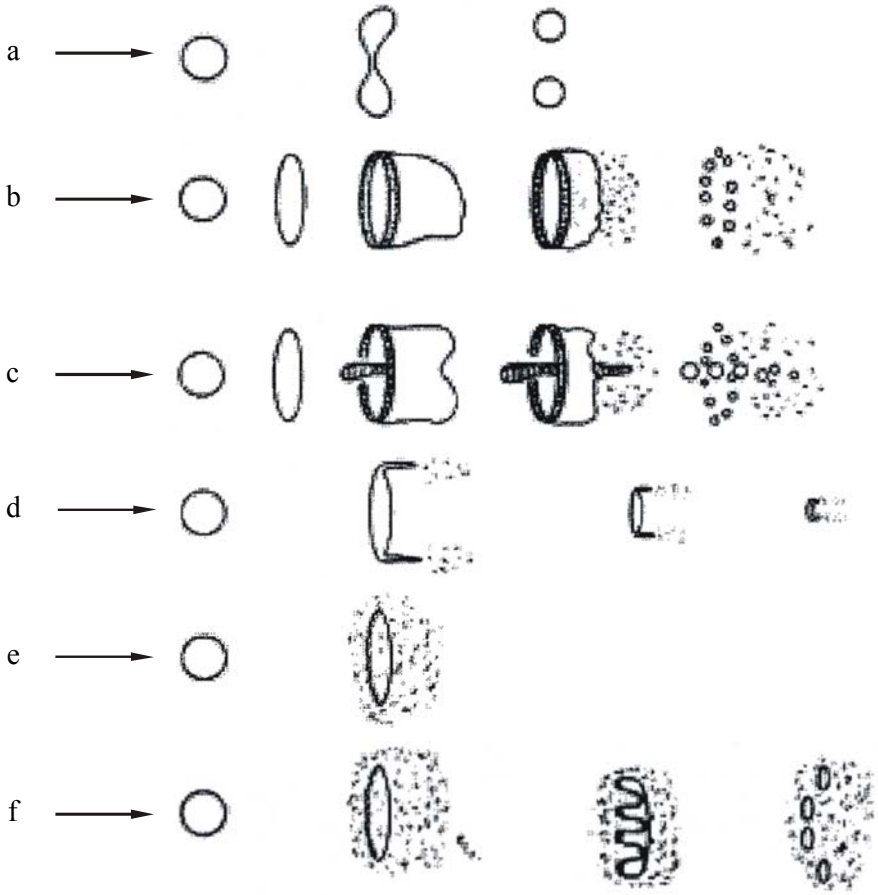

Figure 24: Mechanisms of breakup of low-viscosity liquid drops observed experimentally [151]: (*a*) vibrational breakup We < 12, (*b*) bag breakup 12 < We < 50, (*c*) bag-and-stamen breakup 50 < We < 100, (*d*) sheet stripping 100 < We < 350, (*e*) wave crest stripping 350 < We < 2670, and (*f*) catastrophic breakup We > 2670. Arrow shows the flow direction.

The figure illustrates schematically the sequence of breakup stages representing only their major features, many details remaining beyond the picture. Although the conditions for critical Weber numbers and for each particular breakup mode reported in various publications differ, the discrepancy is not significant to deserve special discussion. In strong SW spreading in sprays, the main droplet breakup mode is combination of stripping (*d*) and Rayleigh–Taylor (*e*) instability modes. These modes produce two sorts of secondary drops: micromist, as a result of disintegration of the stripped sheet, and larger drops arising after perforation of the parent drop with gaseous "fingers" due to Rayleigh–Taylor instability and disintegration of the perforated disc.

As follows from linear analysis, there is a minimum wavelength of instability waves $\lambda_w = 2\pi(\sigma_l / \rho_l a_d)^{1/2}$ (where a_d is the drop acceleration) below which their amplitude does not grow [152], hence drops of size less than λ_w are not subjected to Rayleigh–Taylor instability. According to [152], behind a SW with M = 3.0, λ_w ranges between 23 and 63 μm. Unfortunately, available experimental data pertain to larger drops, therefore breakup patterns of fine drops call for additional experimental verification.

Breakup modes inherent in lower We numbers are important for weak SWs. Usually they do not result in such a dramatic increase of the evaporating surface area as do the stripping and Raileigh–Taylor instability modes. But there is one process where these modes can significantly change the burning process. This is transition from deflagration of a spray to detonation, which is greatly stimulated by sending weak shock waves in a burning spray.

2.4 Cloud of breakup fragments

One of the most important questions relevant to drop ignition phenomenon behind a SW is how fast the fuel is mixed with oxidizer on molecular level. The answer to this question presumes knowledge of (*i*) the total breakup times and (*ii*) state and geometry of the two-phase cloud arising after the breakup. The representative time of drop deformation, and hence breakup, following from dimensional analysis is $t^* = d_s(\rho_l / \rho)^{1/2} / U$; therefore, for convenience the total breakup time is usually expressed in *t** units. The reduced breakup times τ for low-viscosity liquids range between 3.5 and 6. The authors of [151] report empirical formulas relating τ to We number:

$\tau = 6(\mathrm{We} - 12)^{-0.25}$	at	$18 \geq \mathrm{We} \geq 12$
$\tau = 2.45(\mathrm{We} - 12)^{0.25}$	at	$45 \geq \mathrm{We} \geq 18$
$\tau = 14.1(\mathrm{We} - 12)^{-0.25}$	at	$351 \geq \mathrm{We} \geq 45$
$\tau = 0.766(\mathrm{We} - 12)^{0.25}$	at	$2670 \geq \mathrm{We} \geq 351$
$\tau = 5.5$	at	$\mathrm{We} \geq 2670$

Thus, the fluid in the wake of a disintegrated drop is a mixture of the free-stream gas, fuel vapor, and secondary droplets of various sizes. Photographic studies fail to provide information about the state of the material in the drop wake because of strong light scattering by dispersed material, even X-ray diagnostics [153] furnishes data on the overall density of the mixture saying nothing about the structure and aggregate state of the mixture.

Figure 25 shows a photograph of a shattered water drop 0.3 mm in diameter in the shock induced airflow behind the SW of Mach number 2.4. The totally opaque wake of the drop consists of very fine droplets. The amount of air entrained in the wake at τ = 3.1 is estimated at about 450 volumes of the original drop. If it were hydrocarbon drop, rather than water, the equivalence ratio Φ averaged over the wake would be about 5. Based on qualitative understanding of the drop breakup mechanism one can only speculate that the cloud behind the drop has the shape close to conical and the main part of fragments is concentrated at its periphery.

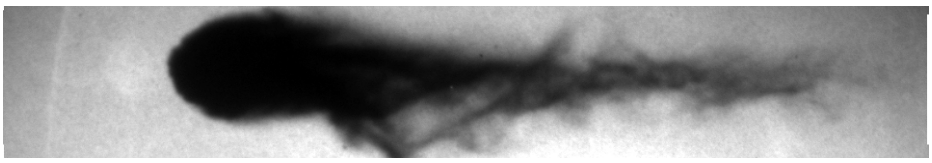

(*a*)

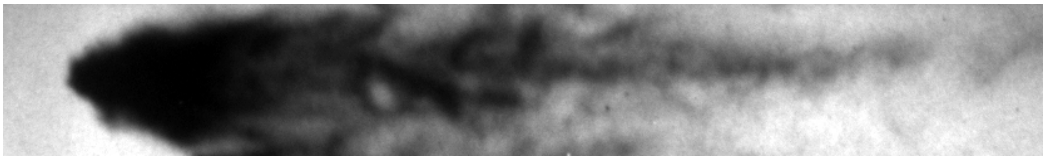

(*b*)

Figure 25: Water drop (0.3 mm in diameter) shattered behind a SW with Mach number 2.4 at 22 (*a*) and 27 (*b*), τ = 2.5 and 3.1, respectively. Initial air pressure is 1 atm.

2.5. Vaporization of drops in clouds

Consider a uniform monodisperse suspension of liquid fuel drops [154, 155]. In such a suspension, all drops have the same diameter and are located at the same distance from each other. Black circles in Figs. 26*a* and 26*b* show schematically the drops distributed equidistantly over the plane. The circumferences around drops characterize the penetration depth of diffusion fluxes, i.e., the conditional boundaries of the regions in which vapor concentration and gas temperature differ from their values in the undisturbed embience. The parameters of the ambience remain stationary until the circumferences do not touch each other (Fig. 26*a*). When the diffusion fluxes from neighboring drops meet each other (Fig. 26*b*), all parameters in the interdrop space start varying in time. Obviously, at the process stage shown in Fig. 26*a*, the spray effects are absent (in the approximation of constant pressure). The spray effects start manifest themselves at the stage shown in Fig. 26*b*.

Due to symmetry considerations, an elementary cell in the form of hexahedron shown by the dashed line in Fig. 26*b* can be constructed around each drop. The mass, momentum, and energy fluxes through the faces of this cell should be evidently zero. The characteristic size of the cell R_c is the half-distance between drops. In the 3D space, the elementary cell has a shape of regular

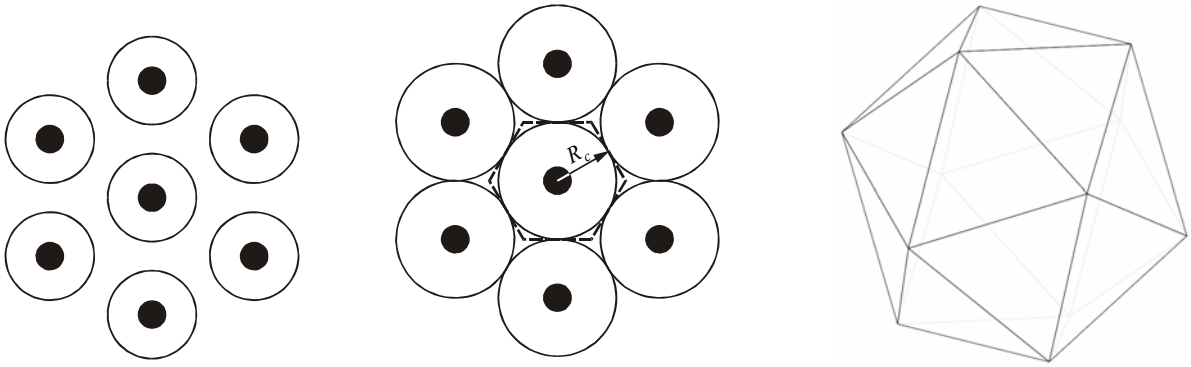

(*a*) (*b*) (*c*)

Figure 26: Elementary cell for the uniform monodisperse drop suspension [154, 155]. Black circles denote drops. Circumferences around drops characterize the spread of diffusion fluxes from individual drops. (*a*) Spray effects are absent; (*b*) spray effects manifest themselves. Dashed line bounds the elementary cell with zero mass end energy fluxes through its surface; R_c is the characteristic cell size (half-distance between drops); and (*c*) 3D elementary cell in the form of a regular polyhedron with 20 faces.

polyhedron with 20 faces in the form of equilateral triangles with the face length R_c (Fig. 26*c*). Thus, drop behavior in the suspension can be modeled by solving the governing conservation equations for a single drop with symmetry boundary conditions at the polyhedron faces. Polyhedron volume and surface area are equal to $V_c = (5\sqrt{2}/3)R_c^3$ and $S_c = 5\sqrt{3}R_c^2$, respectively.

To visualize the flow pattern in such an elementary cell, a transient 3D problem on the flow evolution around a porous sphere modeling an evaporating drop was solved in [154, 155]. The flow field in the computational domain appeared to be very close to the 1D spherically symmetric field. The distortions of the 1D flow field were observed only in the vicinity to the polyhedron vertices where some tangential energy fluxes and insignificant convective flows took place. In view of it, the 3D problem can be reduced to 1D formulation with zero-flux boundary conditions at the surface of the elementary sphere of radius R_{sc}, volume $V_{sc} = (4/3)\pi R_{sc}^3$ and surface area $S_{sc} = 4\pi R_{sc}^2$. Using the condition of equal volumes of elementary sphere and polyhedron $V_{sc} = V_c$ one can readily obtain the radius of elementary sphere as $R_{sc} = (5\sqrt{2}/4\pi)^{1/3} R_c \approx 0.826 R_c$. It appears that the surface areas of the elementary sphere and polyhedron differ only by 1%, i.e., $S_{sc}/S_c \approx 0.99$. Despite the adopted approximation does not take into account the tangential mass, momentum, and energy fluxes existing at the periphery of the polyhedron cell, one can anticipate that the approximate solution of the problem will reflect the main features of heat and mass transfer phenomena in drop suspensions[1].

The statement of 1D spherically symmetrical problem is the same as that reported in [154, 155]. The model is based on nonstationary differential equations of conservation of mass and energy in liquid and gas phases at variable thermophysical properties. In the statements, a concept of multicomponent diffusion of reactive species is used for the mixture containing fuel vapor, oxygen, nitrogen, and various combustion products. The effect of liquid surface tension on drop evaporation rate is also taken into account. The model is formulated for constant-pressure conditions in the gas–drop system, i.e., $p = p_0 = const$.

Initially, at $t = 0$, the radius of elementary polyhedron cell R_c can be found based on the mass content of liquid in the unit volume of drop suspension, $\eta << \rho_l$, and initial drop radius r_{s0}:

$$R_c \approx \left(4\pi/5\sqrt{2}\right)^{1/3} r_{s0} \left(\rho_l/\eta\right)^{1/3} \approx 1.211 r_{s0} \left(\rho_l/\eta\right)^{1/3} \tag{38}$$

or based on the fuel–air ratio $\Phi = \eta/(\phi_{st}\rho)$:

$$R_c \approx \left(4\pi/5\sqrt{2}\right)^{1/3} r_{s0} \left[\rho_l/\left(\rho\Phi\phi_{st}\right)\right]^{1/3} \approx 1.211 r_{s0} \left[\rho_l/\left(\rho\Phi\phi_{st}\right)\right]^{1/3} \tag{39}$$

where ϕ_{st} is the stoichiometric fuel–air ratio[2]. The radius of spherical elementary cell can be derived from Eqs. (38) and (39):

---

[1] Note that these implications are also valid for a localized region in suspension with uniform spatial distribution of monodisperse drops. In realistic nonuniform two-phase flows with polydisperse drops, one can also distinguish localized regions with such prerequisites due to dynamic stratification of drop size fractions.

[2] Parameters η and Φ can be treated as local parameters in nonuniform drop suspensions.

$$R_{sc} \approx r_{s0}(\rho_l / \eta)^{1/3} \approx r_{s0}[\rho_l / (\rho \Phi \phi_{st})]^{1/3} \tag{40}$$

At normal conditions, for stoichiometric mixtures of hydrocarbon fuels with air $\rho = 1.19$ kg/m^3, $\rho_l =$ 700–800 kg/m^3, $\phi_{st} \approx 0.06$ and $\Phi = 1$, hence $\eta = \eta_{st} \approx 0.07$–$0.08$ kg/m^3, $R_c / r_{s0} \approx 25$–27 and $R_{sc} / r_{s0} \approx 21$–$22$. At elevated pressures, for example at the end of compression stroke in a diesel engine, ($\rho_g \approx 30$ kg/m^3) $R_c / r_{s0} \approx 9$ and $R_{sc} / r_{s0} \approx 8$.

Since the statement of the problem implies that $p = const$, parameter R_{sc} (and R_c) is time dependent, i.e., $R_{sc} = R_{sc}(t)$. The value of $R_{sc}(t)$ should be determined in the course of solution allowing the boundary of the spherical elementary cell $r = R_{sc}$ to move with gas. Thus, the boundary conditions at $r = R_{sc}$ are written in the form:

$$r = R_{sc}(t): \quad \frac{\partial \tilde{T}}{\partial r} = 0, \quad \frac{\partial Y_j}{\partial r} = 0 \ (j = 1,2,...,M) \tag{41}$$

where M is the number of gaseous species. The conditions (41) differ from the conditions for a single isolated drop [156] as the mass and energy fluxes vanish at a finite distance $r = R_{sc}$ from the drop rather than at $r \to \infty$.

The initial conditions at $t = 0$ are written as:

$$\begin{gathered} r_s(0) = r_{s0} \\ r < r_{s0}, \quad T(r,0) = T_0 \\ r > r_{s0}, \quad \tilde{T}(r,0) = \tilde{T}_0 \\ r_{s0} < r \le R_{sc}, \quad Y_j(r,0) = Y_{j0} \qquad j = 1, 2, ..., M \end{gathered} \tag{42}$$

Conditions (42) make a provision for nonzero initial vapor content Y_{v0} in the gas phase. For numerical solution of the problem, a finite-difference scheme and iterative procedure are used. The details were reported elsewhere [154–156].

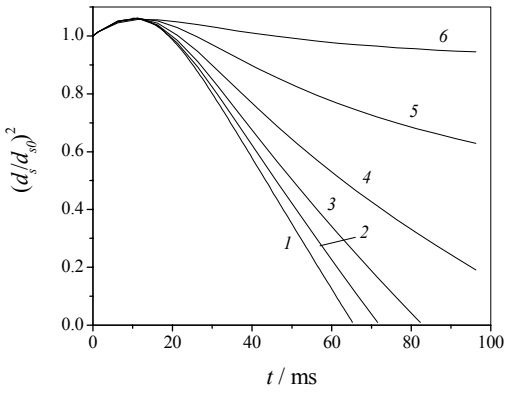

Figure 27: Predicted dynamics of drop surface area for *n*-tetradecane drop suspensions evaporating in air at different fuel – air ratios Φ (distance between drops R_c / r_{s0}) at $d_{s0} = 70$ μm, $T_0 = 293.15$ K, $\tilde{T} = 573.15$ K and $p = 0.1$ MPa [154, 155]. *1* — $\Phi = 0$ ($R_c / r_{s0} \to \infty$), *2* — 0.6 (40.0), *3* — 1.2 (31.5), *4* — 2.4 (25), *5* — 4.75 (20), and *6* — 9.5 (15.7).

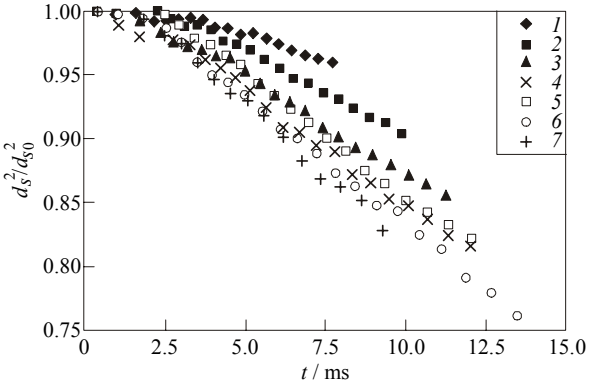

Figure 28: Measured vaporization dynamics of monodisperse ethanol drops in the linear array issued vertically upward along the thermal boundary layer at the vertical heated plate [157]. Points *1–7* correspond to different spacing between drops R_c / r_{s0}: *1* — R_c / r_{s0} = 2.6, *2* — 5, *3* — 7.2, *4* — 9.4, *5*— 11.5, *6* — 13.6, and *7* — 15.8.

Analysis of drop evaporation in dense suspensions shows [154, 155], that the drop vaporization rate and lifetime in suspension may differ considerably compared to those relevant to a single drop placed in an unconfined atmosphere. Figure 27 shows the predicted drop surface regression curves for *n*-tetradecane drops in suspensions of different densities. Three important findings follow from Fig. 27: (1) the account for spray effects results in slower drop vaporization; (2) quasi-steady drop vaporization law is in general not valid; and (3) for each liquid there exists a fuel–air ratio Φ_m (or η_m) such that at $\Phi > \Phi_m$ (or $\eta > \eta_m$) drops evaporate only partly. The first and second findings are confirmed experimentally. For example, Fig. 28 shows the results of measurements [141] of ethanol drop vaporization dynamics in the linear arrays with different spacing between drops. It is seen that a decrease in the drop spacing leads to decrease in the drop vaporization rate just at the beginning of the process and the dependence d_s^2 / d_{s0}^2 on time declines greater from the straight line. Note that the screening effect of neighboring drops in the linear array is considerably smaller that in the schematics of Figs. 26*b* and 26*c*.

It is natural to anticipate that similar effects are inherent in the micromist behind a shattered parent drop. Unfortunately, this stage of the process is not properly studied yet to propose reliable relationships for calculating its rate.

2.6 Kinetic mechanisms of drop ignition and combustion

To study gas-phase autoignition behind SW, detailed reaction mechanisms are widely used. As for the fuel drops and sprays, detailed reaction mechanisms were not used so far except for several recent publications, e.g., [158]. This is caused by the fact that the kinetic mechanisms of high hydrocarbons are very complex and in addition to chemical complications drop combustion is accompanied with complex physical processes. Therefore for modeling *n*-alkane drop ignition and combustion, reduced or overall reaction mechanisms are usually applied [155, 159, 160]. A reaction mechanism in [155, 159, 160] contains 10 reactions with 10 species (fuel, O_2, N_2, CO, CO_2, H_2, H_2O, NO, soot and generalized radical). The mechanism was validated on the problems of premixed laminar flame propagation and laminar counterflow diffusion flame, as well as fuel drop auto-ignition and combustion [155, 159-163]. It was found to be well applicable to description of high-temperature oxidation of *n*-alkanes at temperatures exceeding 1200–1300 K. At temperatures below 900 K the kinetics of *n*-alkane oxidation changes and so-called multistage behavior accelerating the chemical process starts manifesting itself. To model multistage autoignition, more complex kinetic mechanisms are required.

There are several publications on detailed and semiempirical reaction mechanisms for heavy hydrocarbons. For example, in [164] oxidation mechanisms of *n*-heptane and *iso*-octane have been suggested. The mechanism [164] is composed of two reaction blocks: detailed mechanism of C_1-C_2 hydrocarbons oxidation and overall mechanism of low-temperature oxidation and decomposition of *n*-heptane and *iso*-octane. In [165], a kinetic mechanism of low-temperature *n*-tetradecane oxidation has been developed, which is also composed of two reaction blocks. The first block is the detailed reaction mechanism of C_1-C_2 hydrocarbons oxidation. It includes 119 reversible elementary reactions with 29 species. This block is the same as that used in [164]. The second block is the overall mechanism of low-temperature oxidation and decomposition of $C_{14}H_{34}$. It contains 15 reactions with 7 new species.

2.7 High-temperature drop ignition

High-temperature autoignition of *n*-heptane drops was modeled in [155, 159, 160] using the overall kinetic mechanism. For a single drop in microgravity conditions, a satisfactory agreement between predicted and measured [166, 167] ignition delay times was obtained (Table 7). In the calculations, the initial temperature of drops was taken equal to 293 K. The ambient air temperature was assumed to be spatially uniform. The size of the computational domain around the drop R_{sc} was taken sufficiently large as compared with the initial drop radius r_{s0}, so that the values of all parameters on the external boundary were constant in the course of calculations.

Table 7: Comparison of predicted and measured autoignition delay times for isolated *n*-heptane drops at pressure of 0.1 MPa under microgravity conditions [155, 160].

Initial drop diameter, μm	Air temperature, K	t_{ign}, s	
		Measured	Calculated
700	1000	0.30 [166]	0.19
1000	960	0.58 [167]	0.48

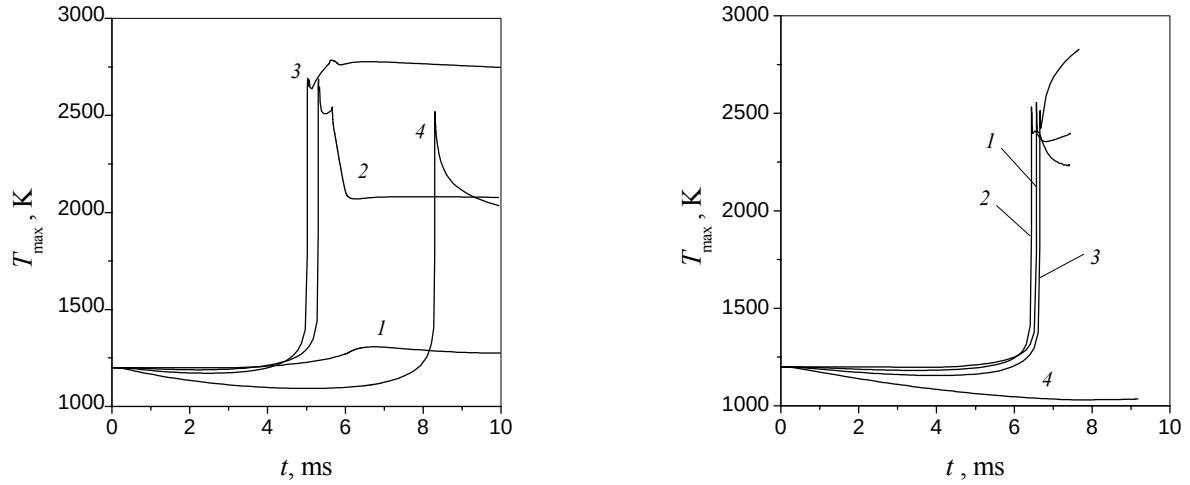

Figure 29: Predicted dependencies of maximal temperature in the vicinity of *n*-heptane (*a*) and *n*-tetradecane (*b*) drops at autoignition conditions. Initial data: $d_{s0} = 50$ μm, $T_0 = 293.15$ K, $\tilde{T} = 1200$ K, $p = 0.1$ MPa. *1* — $\Phi = 0$ (single drop), *2* — 0.5, *3* — 1.0, and *4* — 2.0.

After a certain time referred to as the ignition delay time, t_{ign}, at a certain distance from the drop surface, autoignition of fuel vapor was detected in the calculations. The ignition delay t_{ign} was defined as the time interval taken for the rate of maximal temperature rise to attain a predefined value of $T'_{\max} = 10^6$ K/s. Other reasonable definitions were also used, but they resulted in very similar values of t_{ign}. Figures 29*a* and 29*b* show predicted dependencies of maximal temperature in the vicinity of *n*-heptane (*a*) and *n*-tetradecane (*b*) drop at $T_0 = 293.15$ K, $\tilde{T} = 1200$ K and $p = 0.1$ MPa. A single *n*-heptane drop fails to ignite at these conditions, while a single *n*-tetradecane drop ignites (see curves *1*). Curves *2–4* correspond to $\Phi = 0.5$, 1.0, and 2.0 and demonstrate the spray effect on autoignition of drop suspensions of these two fuels. For *n*-heptane drop suspensions, the shortest ignition delay is attained in the stoichiomentric mixture (curve *3* in Fig. 29*a*). Fuel-rich drop suspensions of *n*-heptane ($\Phi = 2.0$) ignite only after complete drop vaporization. For *n*-tetradecane drop suspensions, the shortest ignition delays are attained in fuel-lean suspensions (curve *2* in Fig. 29*b*, $\Phi = 0.5$). Fuel-rich *n*-tetradecane suspensions ($\Phi = 2.0$) fail to ignite, at least during 10 ms. Thus, autoignition of drop suspensions is very sensitive to suspension density and liquid fuel properties.

Following [159, 160] introduce the concept of normalized mass content of the *j*th species, $I_j(t)$, as the ratio of the total mass of this component in the gas phase at time t to the initial drop mass, $m_0 = (4/3)\pi r_{s0}^3 \rho_l$, i.e.,

$$I_j(t) = m_0^{-1} \int_{r(t)}^{R_{sc}} 4\pi\xi^2 Y_j(\xi,t) d\xi$$

As before, index *v* will be used for fuel vapor. It is instructive to distinguish between fuel, which is initially in the liquid and in the vapor phase. The former and the latter will be marked by indices *vd* and *vg*, respectively. Thus,

$$I_v(t) = I_{vd}(t) + I_{vg}(t)$$

The first term in the right-hand side of this equation relates to the part of I_v corresponding to the fuel, which is initially contained in the liquid drop. The second term relates to the part of I_v , which is initially contained in the vapor phase, e.g., due to preliminary partial drop vaporization. By definition, the prevaporization degree (PD) is equal to $I_{vg}(0)$. The normalized fuel content varies with time due to two processes: drop vaporization and chemical reaction. When liquid drop evaporates completely but fuel does not react chemically, the value of I_{vd} tends to unity. If there are gas-phase reactions of fuel oxidation, then fuel vapor is depleted in the course of reactions and the value of I_v decreases (in case of a single drop, I_v tends to zero).

Figures 30*a* and 30*b* present the example of predicted time histories of a squared drop diameter $d^2(t)$ at autoignition of a single *n*-hexane drop. At completion of ignition delay time (t_{ign}=160 μs) the $d^2(t)$ curve exhibits a fraction and the dependence becomes linear. The drop lifetime is about 250 μs . Figure 30*b* shows the corresponding dependencies $I_v(t)$ for different species: fuel (C_6H_{14}), CO, H_2, CO_2 and H_2O at $I_{vg}(0) = 0$. It is seen that during the ignition delay the fuel vapor accumulates in the gas phase (curve C_6H_{14}). After autoignition, a part of fuel vapor burns out rapidly and then the rate of fuel vapor consumption stabilizes and becomes nearly constant. This stage corresponds to the diffusion-limited combustion of the drop. Carbon dioxide and water accumulate with time while the yields of other products (CO and H_2) are insignificant.

Figure 31*a* shows the predicted time history of the normalized mass content of fuel vapor I_{vd} (at $I_{vg} = 0$) in stoichiometric suspension of fine *n*-heptane drops of initial diameter 2, 4, 6, and 8 μm in air. Such drops exhibit very short velocity relaxation times behind incident SWs. In view of it their ignition can be approximately treated as ignition in a quiescent oxidizing atmosphere. Drops of initial diameter 2 μm first evaporate very fast (t_l = 5.8 μs) and then the normalized fuel vapor content decreases very slowly during 100 μs , i.e., the oxidation reaction is virtually slow. The analysis shows that due to fast drop evaporation the temperature in the elementary sphere of radius R_{sc} around the initial drop decreases by about 300 K, i.e., to the value less than 1225 K. At such a low temperature, the oxidation reaction develops considerably longer than 100 μs . It is seen from Fig. 31*a* that all specific features found for 2-micrometer drops are valid for drops 4, 6, and 8 μm in diameter.

The drop lifetime decreases considerably if the gas phase contains initially fuel vapor, for example, due to partial drop prevaporization. In this case, $I_{vg} \neq 0$. Figure 31*b* shows predicted time histories of I_{vd} for the stoichiometric suspensions of fine *n*-heptane drops of initial diameter 2, 4, 6, and 8 μm in air at $I_{vg}(0) = 0.25$. Such a value of $I_{vg}(0)$ corresponds to the case when 25% of the total fuel mass is initially in the vapor phase.

When comparing Fig. 31*b* and *a* one notices that at $I_{vg} \neq 0$ the $I_{vd}(t)$ curves exhibit a new feature: starting from a certain time instant the value of normalized mass content of fuel decreases drastically, i.e., autoignition occurs. For example, at $I_{vg}(0) = 0.25$ (Fig. 31*b*) the drops of diameter 6 μm are ignited at t = 60 μs due to fast oxidation of prevaporized fuel. After the autoignition event, the rate of fuel burnout slows down and transition to diffusion-controlled drop combustion is observed. At time t = 100 μs , there is only 2.5% unburned fuel. Autoignition of prevaporized fuel in the stoichiometric suspension with drops 8 μm in diameter occurs approximately at the same time: in 60 μs . However, during 100 μs nearly 4.6% fuel remains unburned. Autoignition of drops

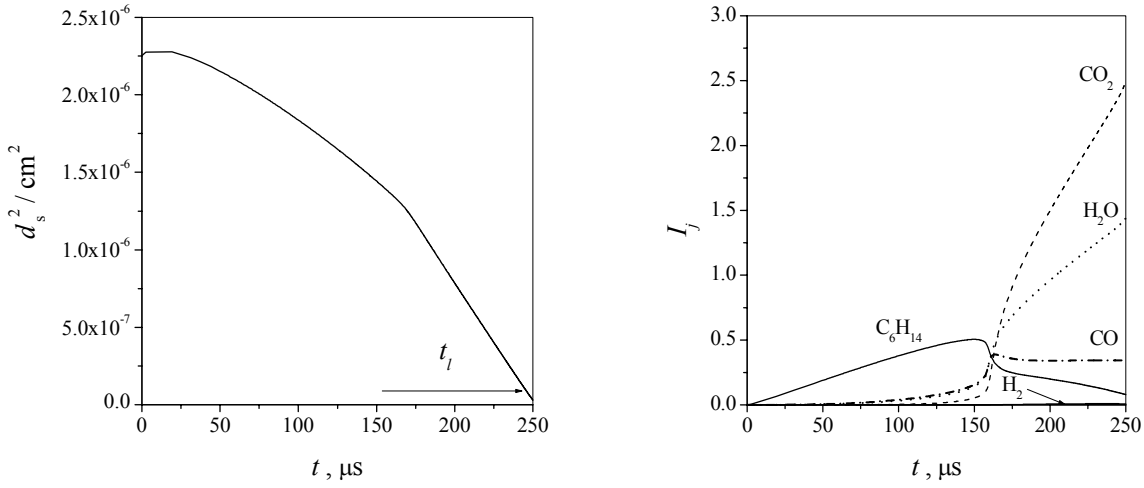

(a) (*b*)

Figure 30: Predicted time histories of a squared *n*-hexane drop diameter (*a*) and normalized mass contents of various combustion products in the gas phase (*b*); t_l is the drop lifetime; d_{s0} = 15 μm, $\tilde{T}$ = 1500 K, and p = 3 MPa [159, 160].

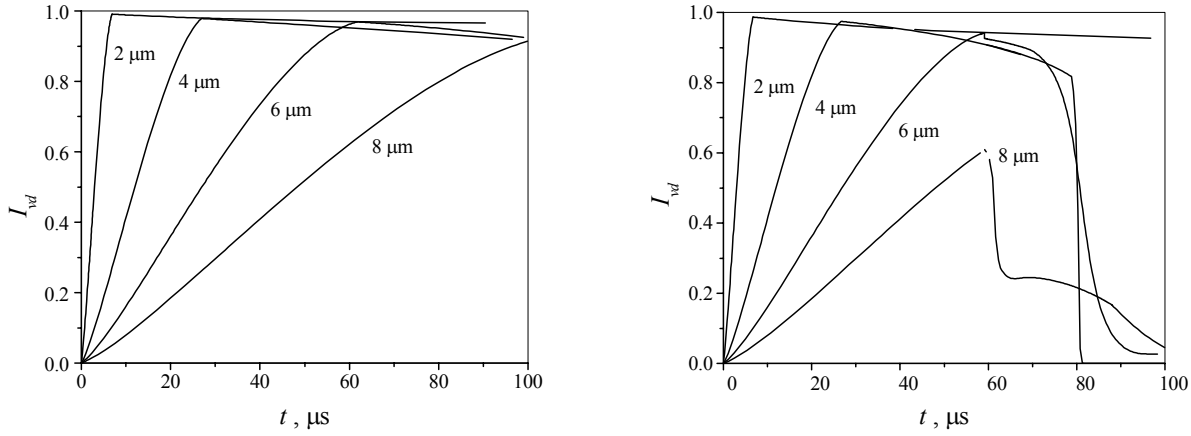

(a) (*b*)

Figure 31: Predicted time histories of normalized mass content of fuel I_{fd} for fine *n*-heptane drops of initial diameter 2, 4, 6, and 8 μm at $\tilde{T}$ = 1500 K and p = 3 MPa: (*a*) I_{fg} = 0, and (*b*) 0.25 [159, 160].

4 μm in diameter occurs with the delay time of about 80 μs (strong influence of initial cooling caused by fast vaporization manifests itself), however, toward the time of 100 μs the fuel is completely burned. Drops 2 μm in diameter are ignited with the ignition delay exceeding 100 μs. The dynamics of suspension ignition changes with increasing PD. At $I_{vg}(0) = 0.5$, the drops 2, 4, and 6 μm in diameter burn out completely during 100 μs, while the 8-micrometer drops burn out only partly: about 2.5% fuel remains unburned. Even at $I_{vg}(0)$ = 0.75, 8-micrometer drops burn out incompletely during 100 μs (about 1.5% fuel remain unburned). It is interesting that larger drops (6 and 8 μm) exhibit combustion modes with several autoignition events [159, 160].

2.8 Low-temperature drop ignition

In the calculations of low-temperature drop autoignition, the semiempirical kinetic mechanism of *n*-tetradecane was used [165]. The calculations were performed for the stoichiometric drop suspension, i.e., the radius of the computational domain R_{sc} around a drop was taken equal to the radius of the stoichiometric elementary sphere.

Figures 32*a* to 32*e* show the examples of predicted time histories of squared drop diameter $(d_s / d_{s0})^2$ (*a*), maximal gas temperature $\tilde{T}_{\max}$ (*b*), normalized mass content of hydroxyl OH (*c* and *d*), and normalized mass contents of alkylhydroperoxide $C_{14}H_{29}O_2H$ and hydrogen peroxide H_2O_2 (*e*) at autoignition of *n*-tetradecane drop with $d_{s0} = 20$ μm at $p = 2.5$ MPa and $\tilde{T} = 650$ K.

Drop lifetime t_l was determined as a time taken for the drop mass to decrease by a factor of 30. The arrow in Fig. 32*a* indicates the calculated drop lifetime with $d_{s0} = 20$ μm ($t_l \approx 1.32$ ms). It is seen from Fig. 32*b* that at the beginning of the process the maximal gas temperature around the drop (at the external boundary of the computational domain) decreases due to drop vaporization and heating. Till time 1.7 ms the value of $\tilde{T}_{\max}$ decreases by about 40 K and further temperature decrease stops due to drop vanishing and a growing heat release caused by chemical reactions. Autoignition occurs in two stages. At first, a cool flame comes into effect after a delay time of $t_{cf} =$ 4.33 ms, which is accompanied with the temperature rise of about 200 K. Then a hot explosion occurs with a total delay time of $t_{\text{ign}} = 4.71$ ms, which is accompanied by the temperature rise to approximately 2200 K.

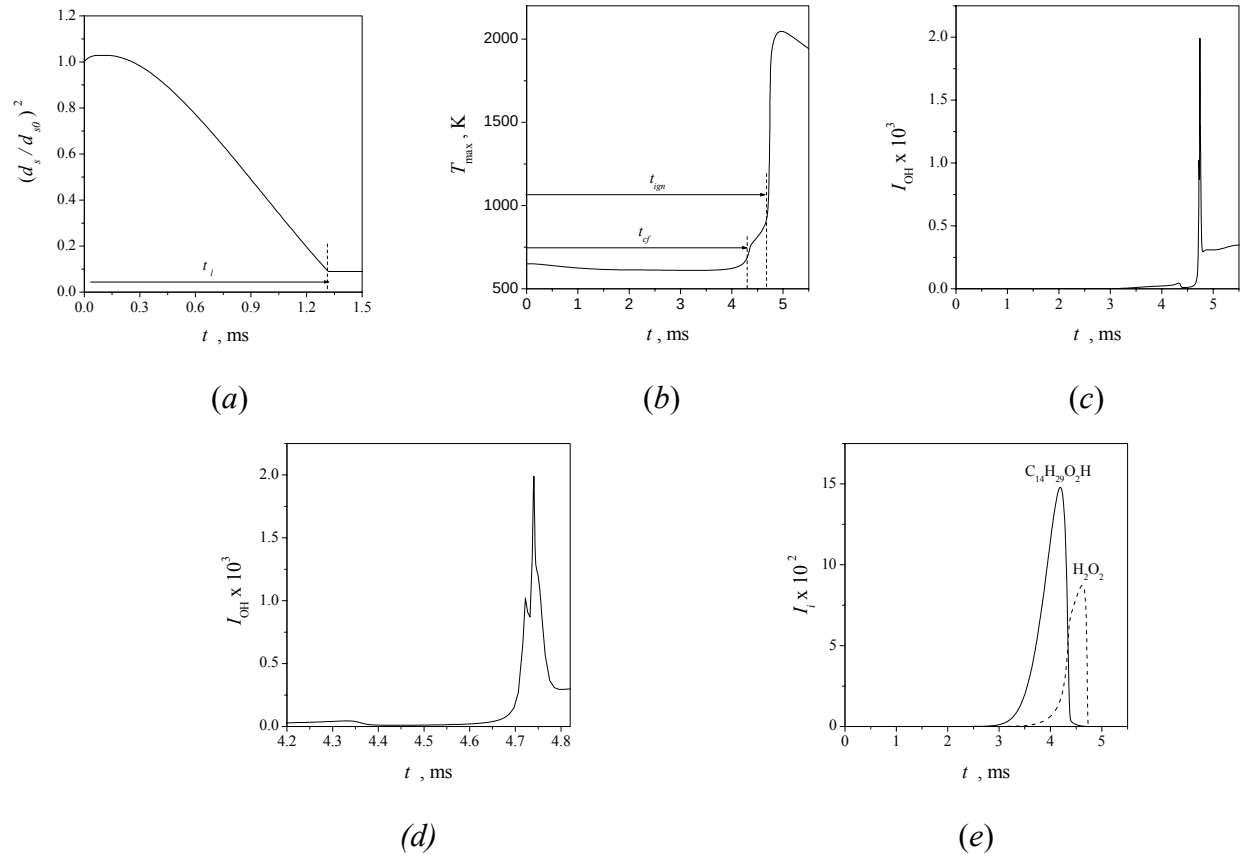

Figure 32: Predicted time histories of the squared drop diameter $(d_s / d_{s0})^2$ (*a*), maximal gas temperature $T_{\max}$ (*b*), normalized mass content of OH (*c* and *d*), and normalized mass contents of alkylhydroperoxide $C_{14}H_{29}O_2H$ and hydrogen peroxide H_2O_2 (*e*) at autoignition of *n*-tetradecane drop with $d_{s0} = 20$ μm ($p = 2.5$ MPa and $\tilde{T} = 650$ K) [165].

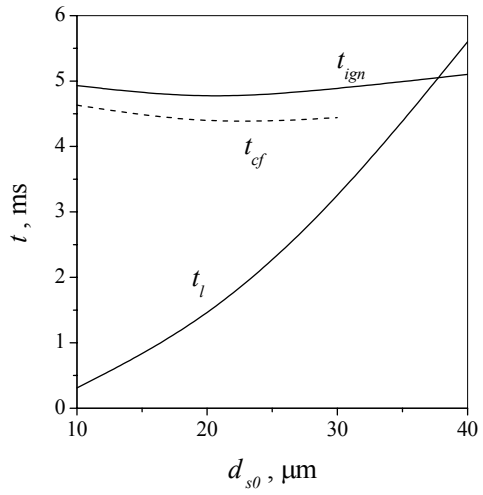

Figure 33: Predicted dependencies of the total ignition delay t_{ign}, ignition delay of the cool flame t_{cf} and drop lifetime t_l on initial drop diameter d_{s0} at p_0 = 2.5 MPa and T_{g0} = 650 K [165].

Comparing Figs. 32*a* and 32*b* one can see that $t_{cf} > t_l$ for the drop with $d_{\text{s0}} = 20$ μm. This means that fine drops completely evaporate before the incipience of the cool flame, and the cool-flame oxidation of fuel vapor proceeds in a relatively large volume. Such conditions are close to the conditions of cool-flame oxidation in a homogeneous mixture, where it was discovered and multiply observed. Further analysis of Figs. 32*b* and *c* or *d* (Fig. 32*d* is the explosive view of Fig. 32*c*), indicates that temperature rise in the cool flame coincides with the hydroxyl concentration build-up. On the other hand, when comparing Figs. 32*c* or 32*d* with Fig. 32*e*, one notices that the build-up of hydroxyl concentration coincides with decomposition of alkylhydroperoxide, $C_{14}H_{29}O_2H$. In homogeneous mixtures, the latter process is responsible for cool flame appearance. Note that at completion of the total ignition delay in Fig. 32*d* (t_{ign} = 4.71 ms) one can clearly see a local maximum in hydroxyl concentration, coinciding with H_2O_2 decomposition (due to reaction $H_2O_2 = OH + OH$ in the block of a detailed reaction mechanism of C_1-C_2 hydrocarbons oxidation). In homogeneous mixtures, this process is responsible for blue flame appearance. The blue flame appearance is not evident on the temperature curve of Fig. 32*b* because it virtually coincides with hot explosion.

Figure 33 presents the predicted dependencies of the total ignition delay t_{ign} and cool flame ignition delay t_{cf} on initial drop diameter d_{s0} at p = 2.5 MPa and $\tilde{T}$ = 650 K. In addition to curves $t_{\text{ign}}(d_{\text{s0}})$ and $t_{cf}(d_{\text{s0}})$, Figure 33 shows the predicted dependence of drop lifetime on the initial drop diameter $t_l(d_{\text{s0}})$. As is seen, $t_{cf} > t_l$ only for drops with $d_{\text{s0}} < 35$ μm. At $d_{\text{s0}} < 35$ μm, the total ignition delay is a weak function of drop diameter and the cool-flame ignition delay t_{cf} is a main contribution to t_{ign}. Note that the use of the temperature curve for determining t_{cf} becomes complicated for drops with $d_{\text{s0}} > 30$ μm because the temperature curve starts to resemble the curve of single-stage high-temperature oxidation.

Consider now the case when $t_{cf} > t_l$ on the example of autoignition of a *n*-tetradecane drop $d_{\text{s0}} = 40$ μm in diameter at p = 2.5 MPa and $\tilde{T}$ = 750 K. It follows from Fig. 34*a* that the total ignition delay in this case t_{ign} = 1.94 ms (shown by arrow). To the instant of autoignition the surface area of the drop decreased by about 20% and nearly 30% of drop mass has evaporated. Cool flame does not manifest itself at the temperature curve $\tilde{T}_{\max}(t)$. It cannot be distinguished on the

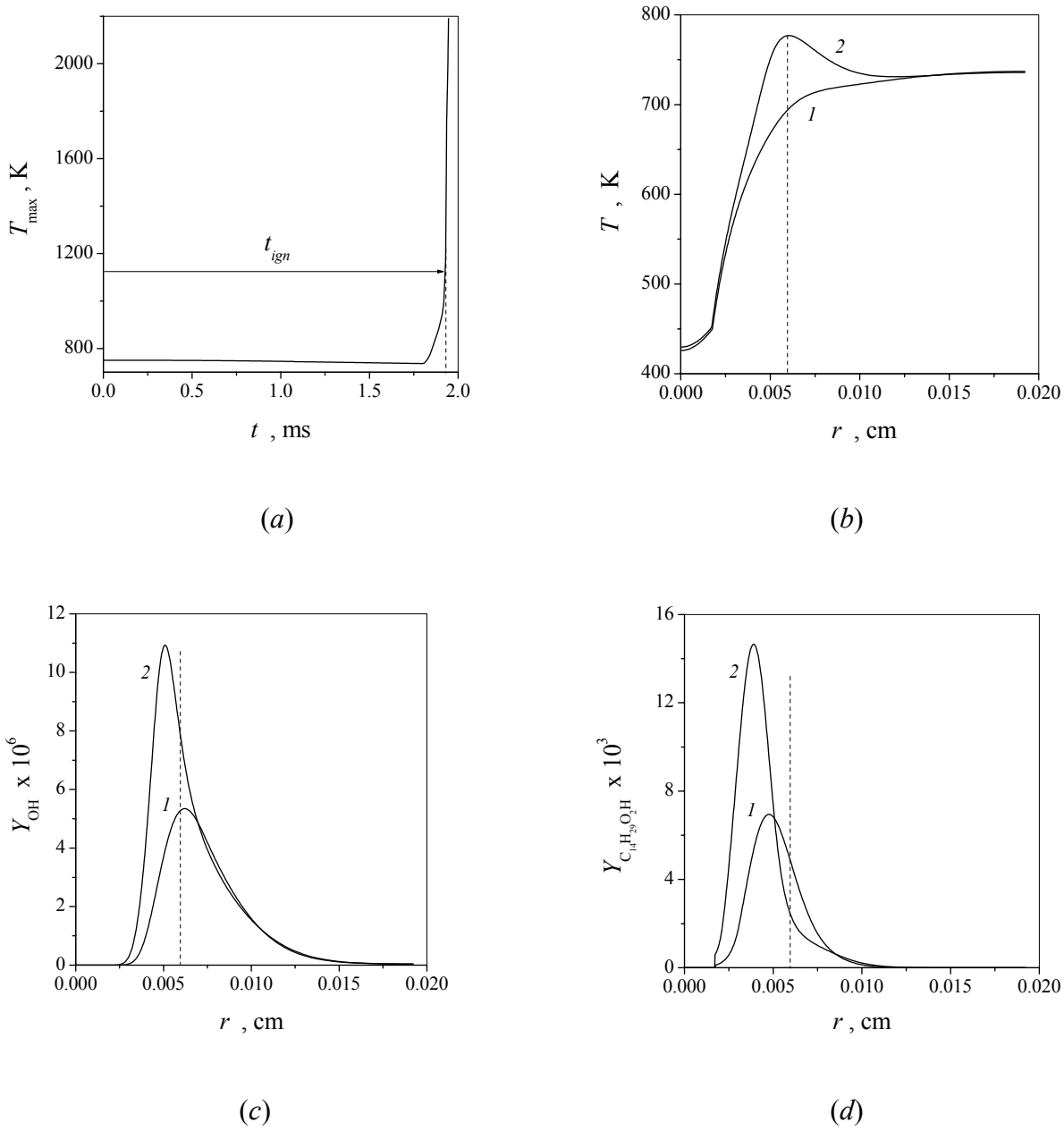

Figure 34: Predicted time histories of maximal gas temperature $T_{\max}$ (*a*) and instantaneous radial distributions of temperature (*b*), mass fractions of hydroxyl Y_{OH} (*c*) and alkyl hydroperoxide $Y_{\mathrm{C_{14}H_{29}O_2H}}$ (*d*) at time t = 1.75 (curves *1*) and 1.85 ms (curves *2*) at *n*-tetradercane drop autoignition (d_{s0} = 40 μm (p_0 = 2.5 MPa and T_{g0} = 750 K) [165].

time histories of normalized mass contents of hydroxyl and alkylhydroperoxide. This is caused by a significant nonuniformity of temperature and concentration field around the drop. Nevertheless, careful analysis of these fields reveals that all features relevant to cool flame development in homogeneous mixtures manifest themselves locally.

Figures 34*b* to 34*d* show the instantaneous radial distributions of temperature (*b*), and mass fractions of hydroxyl Y_{OH} (*c*) and alkylhydroperoxide $Y_{\mathrm{C_{14}H_{29}O_2H}}$ (*d*) at time instants t = 1.75 (curves *1*) and 1.85 ms (curves *2*). It follows from Fig. 34*b* that before ignition, at a time instant between t = 1.75 and 1.85 ms, a localized temperature rise occurs at a distance r = 0.006 cm from the drop center (denoted by the dashed line). This temperature rise corresponds to reaction run-away due to a localized increase in the hydroxyl mass fraction at the same distance from the drop

center (Fig. 34*c*), which, in its turn is caused by a localized decomposition of alkylhydroperoxide (Fig. 34*e*). A special computational experiment indicates that once starting from time t = 1.75 ms the active decomposition products of alkylperoxide in the reaction $C_{14}H_{29}O + OH$ are replaced by considerably less reactive initial species $C_{14}H_{30} + O_2$, the reaction slows down sharply and reaction run-away is replaced by slow-down, and a localized temperature rise is replaced by mixture cooling caused by drop vaporization. Thus, the reaction proceeds in a similar way as in a homogeneous mixture, but locally. This is the reason that the cool-flame stage cannot be distinguished at the time histories of characteristic parameters like maximal temperature of normalized mass contents of various species.

2.9 Ignition of disintegrating drops

A characteristic breakup time of relatively large liquid drops behind strong SW relevant to spray detonations is usually very small as compared to the ignition delay. Whatever the prevailing mechanism of liquid drop atomization behind a SW, ignition occurs in the boundary layer surrounding the drop wake, which, according to experimental observations, is nearly of a conical shape. Thus both numerical simulations and evidence derived from shock tube experiments suggest three major stages of the ignition and combustion process: (*i*) drop breakup, (*ii*) ignition of the mixture at the wake periphery and (*iii*) diffusion controlled fuel burning in the wake.

Which of the stages is rate controlling can be assessed from simple considerations. Breakup of drops 100 μm in diameter is completed within less than 10 μs behind the SW spreading at a velocity of 1600 m/s at atmospheric pressure, the total breakup time of smaller drops is even shorter. However, the pressure measured behind detonation waves in sprays of low-volatility fuels shows that the so-called von Neumann spike where the contribution of the reaction heat to flow characteristics is insignificant lasts no less than 100 μs [168]. Hence, heat release rate behind fuel–air detonation waves in sprays with practically attained drop sizes is controlled by the other two stages.

Mixture autoignition is reasonably assumed to occur at the periphery of the cloud arising in the course of drop breakup because the gas in the wake is colder than the free-stream gas and fuel–oxidizer mixture capable of autoigniting exists only at the boundary between the free-stream and stripped droplet material. Rough estimates [169] show that the amount of fuel mixed with air in this boundary layer is small: no more than 16% over the total breakup time for 100-micrometer particles.

Autoignition in the boundary layer is controlled by chemical kinetics and may occur either after breakup or during it after an induction period, which can be approximately calculated using the free-stream temperature and pressure. For example, Fig. 35 shows the predicted autoignition

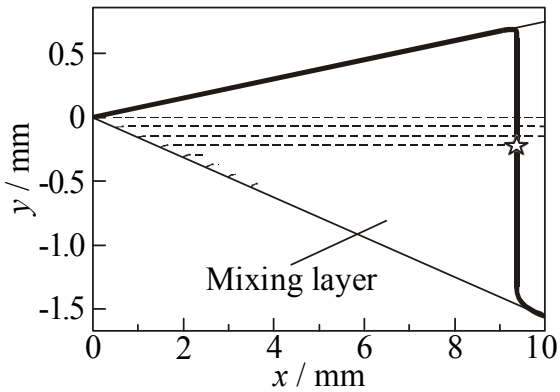

Figure 35: Predicted autoignition location in the planar, isothermal, turbulent mixing layer of a fine fuel spray with air [170, 171]. Thin solid lines show the boundaries of the mixing layer. Thick solid curve denotes the locus of the limiting normalized preexplosion heating $R\tilde{T}/E = 0.05$. Dashed curves show the predicted mean trajectories of notional particles in the mixing layer. Star denotes the self-ignition location, where the notional particle residence time t is equal to ignition delay t_{ign}.

location (denoted by a star) in the planar, isothermal, turbulent mixing layer of a fine fuel spray in air [170, 171]. In the calculations, the following values of governing parameters were used: air density 30 kg/m^3, fuel density 850 kg/m^3, activation energy 8800 cal/mol, temperature 900 K, pressure 4 MPa, and fuel spray velocity at the nozzle exit 100 m/s. Ignition occurs at the periphery of the mixing layer at a distance of about 9 mm from the layer origin and 1.2 mm from the outer (air) boundary of the layer. Although the study in [170, 171] deals with the Diesel spray, the results obtained can be readily applicable to the autoignition phenomenon in the cone-like mixing layer attached to shattered drops behind a SW.

Concluding remarks

Current understanding of physical and chemical processes accompanying solid and liquid particle ignition behind shock waves is based on the simplified treatment of various interactions between particles and the shock induced flow. Analysis of these interactions indicates that the encountered phenomena are very complex and interrelated. Even simple particle/drop ignition models exhibit numerous scenarios of particle/drop temperature evolution behind incident and reflected shock waves. For liquid drops, the phenomena of drop breakup combined with the formation of a mixing layer of micromist droplets with air, micromist vaporization, ignition, and combustion exhibit many features that are not studied yet. The essential role is played by various local rather than averaged processes implying that a multidimensional treatment of the problem is inevitably required.

References

1. Beckstead, M. W.: A summary of aluminum combustion. Paper presented at the *RTO/VKI Special Course on "Internal Aerodynamics in Solid Rocket Propulsion"*, held in Rhode-Saint-Genese, Belgium (27–31 May 2002), and published in RTO-EN 023
2. Law, C. K.: *Prog. Energy Combust. Sci.* **8**, 171 (1982)
3. Sirignano, W. A.: *Prog. Energy Combust. Sci.* **9**, 291 (1983)
4. Bachalo, W. D.: *Proc. 25th Symp. (Intern.) on Combustion*, p. 333. The Combustion Institute, Pittsburgh, PA (1994)
5. Mashayek, F., Pandya, R. V. R.: *Progr. Energy Combust. Sci.* **29**, 329 (2003)
6. Brzustowski, T. A., Glassman, I.: In: Wolfhard, H. G., Glassman, I., Green, L. (eds.) *Heterogeneous Combustion,* pp. 75–115. Academic Press, New York (1964)
7. Klyachko, L. A.: *Teploenergetika* **8**, 20 (1966)
8. Khaikin, B. I., Bloshenko, V. N., Merzhanov, A. G.: *Combust. Explosion Shock Waves* **6**, 412 (1970)
9. Aldushin, A. P., Bloshenko, V. N., Seplyarskii, B. S.: *Combust. Explosion Shock Waves* **9**, 423 (1973)
10. Law, C. K.: *Comb. Sci. Technol.* 7, 197 (1973)
11. Varshavskii, G. A.: *Trans. NII-1* **6**, 30 (1945)
12. Godsave, G. A. E.: Studies of the combustion of drops in a fuel spray – the burning of single drops of fuel. In: *Proc. 4th Symposium (Intern.) on Combustion,* pp. 818–830. Williams and Wilkins, Baltimore, MD (1953)
13. Spalding, D. B.: The combustion of liquid fuels. In: *Proc. 4th Symposium (Intern.) on Combustion,* pp. 847–864. Williams and Wilkins, Baltimore, MD (1953)
14. Goldsmith, M., Penner, S. S.: *Jet Propulsion* **24**(4), 245 (1954)
15. Frank-Kamenetskii, D. A.: *Diffusion and Heat Transfer in Chemical Kinetics*. Nauka, Moscow (1961)
16. Twardus, E. M., Brzustowski, T. A.: *Archiwum Processov Spalania* **8**, 347 (1977)
17. Dwyer, H. A., Nirschl, H., Kerschl, P., *et al*.: In: *Proc. 25th Symp. (Intern.) on Combustion,* pp. 389–396. The Combustion Institute, Pittsburgh, PA (1994)
18. Marberry, M., Ray, A. K., Leung, K.: *Combust. Flame* **57**, 237 (1984)
19. Sivasankaran, K., Seetharamu, K. N., Natarajan, R.: *Int. J. Heat and Mass Transfer* **39**, 3949 (1996)
20. Chiu, H. H., Liu, T. M.: *Combust. Sci. Technol.* **17**, 127 (1977)
21. Correa, S. M., Sichel, M.: In: *Proc. 19th Symp. (Intern.) on Combustion,* pp. 856–863. The Combustion Institute, Pittsburgh, PA (1983)
22. Nigmatulin, R. I.: *Dynamics of Multiphase Media*, Vol. 1. Nauka, Moscow (1987)
23. Borisov, A. A., Kogarko, S. M., Kozenko, V. P.: *Combustion, Explosions, Shock Waves* **2**, 55 (1967)
24. Nettleton, M. A., Stirling, R.: *Proc. Royal Soc. A* **300**, 62 (1967)
25. Macek, A., Semple, J. M.: *Combust. Sci. Technol.* **1**, 181 (1969)
26. Ryzhik, A. B., Yurmanov, Yu. A., Limonov, B. S., *et al*.: *Physics of Aerodispersed Systems* **9**, 115 (1973)
27. Fox, T. W., Rackett, C. W., Nicholls, J. A.: Shock wave ignition of magnesium powders. In: *Proc. 11th Int. Shock Tubes and Waves Symp.,* pp. 262–268. Seattle, WA (1978)
28. Cohen, A., Decker, L.: Shock tube ignition of nitrocellulose and nitramines. In: *Proc. 10th JANAF Meeting* (1978)
29. Cohen, A., Decker, L.: Shock tube ignition of nitrocellulose. In: *Proc. 12th Symp. (Intern.) Shock Tubes,* pp. 514–520 (1979)
30. Kauffman, C. W., Wolanski, P., Ural, E., *et al*.: Shock wave initiated combustion of grain dust. In: *Proc. Symp. (Intern.) on Grain Dust,* pp. 164–190. Manhattan, Kansas (1979)
31. Breipohl, G., Lester, T. W., Merklin, J. F.: Shock tube studies of the mechanism of grain dust ignition. In: *Proc. Symp. (Intern.) on Grain Dust,* pp. 191–211. Manhattan, Kansas (1979)

32. Seeker, W. R., Lester, T. W., Merklin, J. F.: *Rev. Sci. Instr.* **51**(11), 1523 (1980)
33. Ural, E. A., Sichel, M., Kauffman, C. W.: Shock wave ignition of pulverized coal. In: Treanor, C. E., Hall, J. G. (eds.) *Shock Tubes and Waves*, pp. 809–817. State Univ. of New York Press, Albany, New York (1981)
34. Wolanski, P.: Problems of dust explosions. In: *Proc. 1st Specialists Meeting (Intern.) of the Combustion Institute,* pp. 497–502. Bordeaux, France (1981)
35. Wolanski, P.: Fundamental problems of dust explosions. In: Lee, J. H. S., Guirao C. M. (eds.) *Fuel–Air Explosions,* pp. 349–373. Univ. of Waterloo Press, Waterloo (1982)
36. Borisov, A. A., Gelfand, B. E., Tsyganov, S. A., *et al*.: *Chemical Physics Reports* **2**(8), 40 (1983)
37. Borisov, A. A., Gelfand, B. E., Timofeev, E. I., *et al*.: Ignition of dust suspensions behind shock waves. In: Bowen, J. R., Manson, N., Oppenheim, A. K., Soloukhin, R. I. (eds.) *Dynamics of Shock Waves, Explosions, and Detonations*, Progress in Astronautics and Aeronautics, vol. 94, pp. 332–339. AIAA Inc., NY (1984)
38. Sichel, M., Baek, S. W., Kauffman, C. W., *et al*.: *AIAA J.* **23**(9), 1374 (1985)
39. Boiko, V. M., Lotov, V. V., Papyrin, S. V.: *Archivum Combustionis* **8**(2), 101 (1988)
40. Li, S. C., Williams, F. A., Takahashi, F.: In: *Proc. 22nd Symposium (Intern.) on Combustion,* pp. 1951–1960. The Combustion Institute, Pittsburgh, PA (1988)
41. Wolanski, P.: Deflagration and detonation combustion of dust mixtures. In: Kuhl, A. L., Leyer, J.-C., Borisov, A. A., Sirignano, W. A. (eds.) *Dynamics of Deflagrations and Reactive Systems: Heterogeneous Combustion*, Progress in Astronautics and Aeronautics, vol. 132, pp. 3–31. AIAA Inc, NY (1991)
42. Boiko, V. M., Papyrin, S. V., Poplavskii, S. V.: *Combustion, Explosions, Shock Waves* **29(**3), 389 (1993)
43. Boiko, V. M., Papyrin, S. V., Poplavskii, S. V.: Ignition mechanism of coal suspension in shock waves. In: Kuhl, A. L., Leyer, J.-C., Borisov, A. A., Sirignano, W. A. (eds.) *Dynamic Aspects of Explosion Phenomena*, Progress in Astronautics and Aeronautics, vol. 154, pp. 278–290. AIAA Inc, NY (1993)
44. Roberts, T. A., Burton, R. L., Krier, H.: *Combust. Flame* **92**(1–2), 125 (1993)
45. Geng, J. H., van de Ven, A., Zhang, F., *et al*.: A new setup to measure ignition delay of a dust suspension behind and incident shock wave. In: Xufan, D., Wolanski, P. (eds.) *Proc. 6th Colloq. (Intern.) on Dust Explosions,* pp. 309–314. Northeastern Univ Press, Shenyang (1994)
46. Spalding, M. J., Krier, H., Burton, R. L.: *Combust. Flame* **120**, 200 (2000)
47. Servaites, J., Krier, H., Melcher, J. C., *et al*.: *Combust. Flame* **125**, 1040 (2001)
48. Dreizin, E. L., Trunov, M. A., Suslov, A. V.: *Combust. Sci. Technol.* **90**, 79 (1993)
49. Dreizin, E. L., Trunov, M. A.: *Combust. Flame* **101**, 378 (1995)
50. Dreizin, E. L.: *Combust. Flame* **105**, 541 (1996)
51. Molodetsky, I. E., Vicenzi, E. P., Law, C. K., e*t al*.: *Combust. Flame* **112**, 522 (1998)
52. Dreizin, E. L.: *Combust. Flame* **116**, 323 (1999)
53. Dreizin, E. L., Berman, C. H., Vicenzi, E. P.: *Combust. Flame* **122**, 30 (2000)
54. Trunov, A., Schoenitz, M., Zhu, X., *et al*.: *Combust. Flame* 140, 310 (2005)
55. Takeno, T., Yuasa, S.: *Combust. Sci. Technol.* **21**, 109 (1980)
56. Fassel, W. M., Papp, C. A., Hildenbrand, D. L., *et al*.: In: Summerfield, M. (ed.) *Solid Propellant Rocket Research*, pp. 259–269. Academic Press, NY (1960)
57. Gusachenko, E. I., Stesik, L. N., Fursov, V.P., *et al.*: *Combustion, Explosions Shock Waves* **10**, 548 (1974)
58. Shevtsov, V. I., Fursov, V. P., Stesik, L.N.: *Combustion Explosions Shock Waves* **12**, 859 (1976)
59. Cassel, H. V., Liebman, I.: *Combust. Flame* **3**(4), 467 (1959)
60. Cassel, H. V., Liebman, I.: *Combust. Flame* **7**, 1 (1963)
61. Lermant, J. C., Yip, S.: *Combust. Flame* **7**, 1 (1963)
62. Gurevich, M. A., Stepanov, A. M.: *Combustion Explosions Shock Waves* **3**, 334 (1968)

63. Gurevich, M. A., Stepanov, A. M.: *Combustion Explosions Shock Waves* **4**, 189 (1970)
64. Khaikin, B. I., Bloshenko, V. I., Merzhanov, A. G.: *Combustion Explosions Shock Waves* **4**, 474 (1970)
65. Ezhovsky, G. K., Mochalova, A. S., Ozerov, E. S., *et al.*: Ignition and combustion of magnesium particle. In: *Combustion and Explosion,* pp. 234–240. Nedra, Moscow (1972)
66. Ezhovsky, G. K., Ozerov, E. S.: *Combustion Explosions Shock Waves* **6**, 845 (1974)
67. Gremyachkin, V. M., Istratov, O. I.: *Combustion Explosions Shock Waves* **11**, 366 (1974)
68. Bloshenko, V. I., Merzhanov, A. G., Khaikin, B. I.: *Combustion Explosions Shock Waves* **5**, 682 (1976)
69. Derevyaga, M. V., Stesik, L. N., Fedorin, N. A.: *Combustion Explosions Shock Waves* **6**, 44 (1978)
70. King, M. K.: Modeling of single-particle aluminum combustion in O_2–N_2 atmospheres. In: *Proc. 17th Symp. (Intern.) on Combust.,* pp. 1317–1328. The Combustuion Institute, Pittsburgh, PA (1979)
71. Fursov, V. I., Shevtsov, V. I., Gusachenko, E. I., *et al*.: *Combustion Explosions Shock Waves* **3**, 3 (1980)
72. Medvedev, A. E., Fedorov, A. V., Fomin, V. M.: *Combustion Explosions Shock Waves* **3**, 5 (1982)
73. Medvedev, A. E., Fedorov, A. V., Fomin, V. M., *et al*.: Mathematical modeling of ignition process of aerodispersed systems. In: *Proc. 3rd Intern. School of Industrial Dust Explosions,* pp. 65–79. Turava, Poland (1982)
74. Boiko, V. M., Fedorov, A. V., Fomin, V.M., *et al*.: Ignition of small solid Particles behind shock waves. In: Bowen, J. R., Manson, N., Oppenheim, A. K., Soloukhin, R. I. (eds.) *Shock Waves, Explosions, and Detonations*, vol. 87, pp. 71–87. Progress in Astronautics and Aeronautics AIAA Inc, NY (1983)
75. Kazakov, Yu. V., Medvedev, A. E., Fedorov, A. V., *et al*.: *Archivum Combustionis* 7(1–2), 7 (1987)
76. Fedorov, A. V., Tetenov, E. V., Veyssiere, B.: *Combustion Explosions Shock Waves* **5**, 16 (1991)
77. Petukhova, E. V., Fedorov, A. V.: *Combustion Explosions Shock Waves* **6**, 139 (1991)
78. Fedorov, A. V.: Physical and Mathematical Modeling of Ignition of Fine Magnesium Particles. Preprint No. 12-94, pp. 1–30. Inst. Theor. Appl. Mech. SB RAS, Novosibirsk (1994)
79. Makino, A.: *Combust. Flame* **90**, 143(1992)
80. Zhou, W., Yetter, R. A., *et al*.: In: *Proc. 26th Symp. (Intern.) on Combustion,* pp. 1909–1914. The Combustion Institute, Pittsburgh, PA (1996)
81. Hayhurst, A. N.: *Combust. Flame* **121**, 679 (2000)
82. Foertsch, D., Schnell, U., Hein, K.R.G., *et al*.: *Combust. Flame* **126**, 1662 (2001)
83. Tao, H.: *J. de Physique IV* **12**(7), 105 (2002)
84. Meinkoh, D.: *Combust. Theory Modelling* **8**, 315 (2004)
85. Vilyunov, V. N.: *Theory of Ignition of Condensed Substances.* Nauka, Novosibirsk (1984)
86. Gosteev, Yu. A., Fedorov, A. V.: *Combustion Explosions Shock Waves* **32**(4), 5 (1996)
87. Borovikov, M. B., Goldschleger, U. I.: *Doklady USSR Acad. Sci.* **261**(2), 392 (1981)
88. Meinkoehn, D.:Metal particle ignition and oxide layer instability. In: Borisov, A., Frolov, S., Kuhl, A. (eds.) *Progress in Combustion and Detonation*, pp 180–181. Torus Press, Moscow (2004)
89. Ranz, W. E., Marshall, W.R.: *Chem. Eng. Prog.* **48**, 141 (1952)
90. Avdeev, K. A., Frolov, F. S., Frolov, S. M.: Effect of transient heat transfer on metal particle ignition. In: Roy, G., Frolov, S., Sinibaldi, J. (eds.) Pulsed and Continuous Detonations, pp. 72–83. Torus Press, Moscow (2006)
91. Avdeev, K. A., Frolov, F. S., Frolov, S. M., Basara, B.: Effect of transient heat transfer on metal particle ignition. In: Hanjalic, K., Nagano, Y., Jakirlic, G. (eds.) *Turbulence, Heat and Mass Transfer*, Vol. 5, pp. 581–584. Begell House Publ. (2006)

92. Gilmore, R.: *Catastrophe Theory for Scientists and Engineers.* Wiley-Interscience, New York (1981)
93. Fedorov, A. V.: *Combustion Explosions Shock Waves* **1**, 75 (1996)
94. Merzhanov, A. G.: Thermal theory of metal particle ignition," *AIAA J.,* **13**(2), 209–214 (1975)
95. Grigor'ev, Yu. M., Vakina, Z. G.: Critical ignition conditions for metals with a logarithmic oxidation law. *Combustion Explosions Shock Waves* **15**(1), 51–53 (1979)
96. Alekseeva, T. I., Gurevich, M. A., Ozerov, E. S.: Ignition of an aluminum particle. In: *Tr. Leningrad. Politekh. Inst.* **280**, 98–106 (1967)
97. Gurevich, M. A., Ozerov, E. S., Yurinov, A. A.: Effect of an oxide film on the inflammation characteristics of aluminum. *Combustion Explosions Shock Waves* **14(**4), 448–451 (1978)
98. Gurevich, M. A., Ozerova, G. E., Stepanov, A. M.: Heterogeneous ignition of an aluminum particle in oxygen and water vapor. *Fiz. Goreniya Vzryva* **6**(3), 326–335 (1970)
99. Friedman, R., Macek, A.: Ignition and combustion of aluminum particles in hot ambient gases. *Combust. Flame* **6**, 9–19 (1962)
100. Pokhil, P. F., Belyaev, A. F., Frolov, Yu. V., *et al*.: *Combustion of Powdered Metals in Active Media*. Nauka, Moscow (1972)
101. Boiko, V. M., Lotov, V. V., Papyrin, A. N.: Ignition of gas suspensions of metallic powders in reflected shock waves. *Combustion Explosions Shock Waves* **25**(2), 193–199 (1989)
102. Gurevich, M. A., Lapkina, K. I., Ozerov, E. S.: Limiting ignition conditions of an aluminum particle. *Fiz. Goreniya Vzryva* **6**(2), 172–176 (1970)
103. Fedorov, A. V., Kharlamova, Yu. V.: Ignition of an aluminum particle. *Combustion Explosions Shock Waves* **39**(5), 65–68 (2003)
104. Grigor'ev, Yu. M., Gal'chenko, Yu. A., Merzhanov, A. G.: Investigation of the rate of the high-temperature reaction between aluminum and oxygen using the ignition method. *Combustion Explosions Shock Waves* **9**(2), 162–167 (1973)
105. Gear, C. W.: The automatic integration of ordinary differential equations. *Comput. Struct.* **20**(6), 915–920 (1985)
106. Afanasieva, K. A., Levin, V. A.: *Chemical Physics Reports* **3**(9), 1328 (1984)
107. Fedorov, A. V., Tetenov, E. V., Veyssiere, B.: Dynamics and ignition of metal particles dispersed in atmosphere at a real explosion. Preprint No. 6-90, Inst. Theor. Appl. Mech. SB RAS, Novosibirsk (1990)
108. Boiko, V. M., Papyrin, A. N.: On the ignition of magnesium particles behind reflected shock waves. In: *Proc. VIII All-Union Symp. Combustion and Explosion,* pp. 65–68. Chernogolovka, USSR (13–17 Oct 1986)
109. Rosenband, V.: *Combust. Flame* **137**, 366 (2004)
110. Yanenko, N. N., Soloukhin, R. I., Fomin, V. M., *et al*.: *Supersonic Two-Phase Flows in Conditions of the Particles Velocity Non-Equilibrium.* Nauka, Novosibirsk (1980)
111. Zubarev, V. N., Kozlov, A. D., Kuznetsov, V. M., *et al.* Thermophysical properties of technically important gases. Reference book, p. 232. Moscow, Energoatomizdat (1989)
112. Fedorov, A. V.: *Combustion Explosions Shock Waves* **34**(4), 57 (1998)
113. Matsko, A. M., Kopeika, K. M., Polishchuk, D. I., *et al.*: Effect of external heat transfer on the critical conditions for ignition of gaseous suspension of magnesium particles. The Physics of Aerodispersed Systems **20**, 53–56 (1980)
114. Medvedev, A. E., Fedorov, A. V., Fomin, V. M.: Ignition of metal particles in high-temperature flow behind the shock wave. Preprint No. 33. Inst. Theor. Appl. Mech. of the USSR Acad. Sci. Siberian Branch, Novosibirsk (1981)
115. Fedorov, A. V., Fomin, V. M.: Modeling of detonation flows in reacting gas-particle mixtures. In: Borisov, A., Frolov, S., Kuhl, A. (eds.) *Progress in Combustion and Detonation*, pp. 329–330. Torus Press, Moscow (2004)
116. Fedorov, A. V., Fomin, V. M.: J. *Appl. Mech. Techn. Phys.* **40**(2), 128 (1999)

117. Fedorov, A. V., Gosteev, Yu. A.: A numerical study of ignition of magnesium samples in spherical and cylindrical symmetry. In: *Proc. 16th Intern. Colloquium on the Dynamics of Explosions and Reactive Systems,* pp. 299–302. AGH, Cracow, Poland (1997)
118. Gosteev, Yu. A., Fedorov, A. V.: *Combustion Explosions Shock Waves* **35**(5), 38 (1999)
119. Gosteev, Yu. A., Fedorov, A. V.: *Combustion Explosions Shock Waves* **33**(6), 30 (1999)
120. Gosteev, Yu. A., Fedorov, A. V.: *Combustion Explosions Shock Waves* **34**(6), 29 (1998)
121. Wierzba, A.: *Experiments in Fluids* **9**, 59 (1990)
122. Gelfand, B. E., Gubin, S. A., Kogarko, S. M.: *Engineering Physical J.* **25**(3), 17 (1974)
123. Olim, M., Igra, O., Mond, M., *et al*.: In: Groenig, H. (ed.) *Shock Tubes and Waves*, pp. 217–225. HI Publ., Aachen (1987)
124. Simpkins, P. G., Bales, E. L.: *J. Fluid Mechanics* **55**, 4 (1972)
125. Boiko, V. M., Papyrin, A. N., Poplavskii, S. V.: *J. Appl. Mech. Techn. Physics* **2**, 70 (1987)
126. Wadewitz, A., Specht, E.: *Int. J. Heat and Mass Transfer* **44**, 967 (2001)
127. Gordon, G. D.: *J. Appl. Physics* **30**, 11 (1959)
128. Volynskii, M. S., Lipatov, A. S.: *Engineering Physical J.* **18**(5) (1970)
129. Davidson, V. E.: In: Belyaev, N. M., *et al.* (eds.) *Jets and Flow in Tubes*, pp. 3–35. Dnepropetrovsk, USSR (1974)
130. Detkovskii, D. A., Frolov, S. M.: *J. Appl. Mech. Techn. Physics* **4**, 105 (1994)
131. O'Rourke, P. J., Amsden, A. A.: SAE Paper 872089 (1987)
132. Borisov, A. A., Gelfand, B. E., Gubin, S. A., *et al*.: *Combustion Explosions Shock Waves* **3**, 374 (1970)
133. Zhdan, S. A.: *Combustion Explosions Shock Waves* **12**(4), 586 (1976)
134. Eidelman, S., Burkat, A.: *AIAA J.* **18**(9), 1103 (1980)
135. Burkat, A., Eidelman, S.: *AIAA J.* 18(10), 1233 (1980)
136. Sichel, M.: In: Oran, E. S., Boris, J. P. (eds.) *Numerical Approaches to Combustion Modeling*, vol. 135, pp. 447–458. Progress in Astron. Aeron., AIAA Inc, NY (1991)
137. Gubin, S. A., Sichel, M.: *Combust. Sci. Technol.* **17**(3-4), 109 (1977)
138. Borisov, A. A., Gelfand, B. E.: *J. Appl. Mech. Techn. Physics* **5**, 85 (1970)
139. Borisov, A. A., Gelfand, B. E., Gubin, S. A., *et al*.: *Astronautica Acta* **15**, 411 (1970)
140. Zhdan, S. A.: *Combustion Explosions Shock Waves* **13**(2), 258 (1977)
141. Zhdan, S. A., Voronin, D. V.: *Combustion, Explosion, Shock Waves* **20**(4), 112 (1984)
142. Prakash, S., Sirignano, W. A.: *J. Heat Mass Transfer* **21**, 885 (1978)
143. Smetanyuk, V. A., Frolov, S. M.: *Khimicheskaya Fizika* **23**(7), 40 (2004)
144. Helenbrook, B. T., Edwards, C. F.: *Int. J. Multiphase Flow* **28**, 1631 (2002)
145. Frolov, S. M., Smetanyuk, V. A.: *Khimicheskaya Fizika* **4** (2006)
146. Frolov, S. M., Frolov, F. S., Basara, B.: Mathematical model for transient droplet vaporization. In: Roy, G., Frolov, S., Starik, A. (eds.) *Nonequilibrium Processes. Combustion and Detonation*, vol. 1, pp. 179–193. Torus Press, Moscow (2005)
147. Dukowicz, J. K.: Informal Report Los Alamos Sci. Lab. LA7997-MS (1979)
148. Liu, A. B., Reitz, R. D.: SAE Paper 930072 (1993)
149. Clift, R., Grace, J. R., Weber, M. E.: *Bubbles, Drops and Particles.* Academic Press, NY (1978)
150. Frolov, S. M., Posvianskii, V. S., Basevich, V. Ya., *et al*.: *Khimicheskaya Fizika* **23**(4), 75 (2004)
151. Pilch, M., Erdman, C.: *Int. J. Multiphase Flow* **13**, 741 (1987)
152. Joseph, D. D., Belanger, J., Beavers, G. S.: http://www.aem.umn.edu/research/Aerodynamic_Breakup/
153. Reinecke, W. G., Waldman, G. D.: Technical Report SAMSO-TR-70142, Avco Systems Division (1970)
154. Frolov, S. M., Basevich, V. Ya., Posvianskii, V. S., *et al*.: *Khimicheskaya Fizika* **23**(7), 49 (2004)

155. Frolov, S. M., Basevich, V. Ya., Belyaev, A. A., *et al*.: Modeling of drop vaporization and combustion with regard for spray effects. In: Roy, G. D., Frolov, S. M., Starik, A. M. (eds.) *Combustion and Pollution: Environmental Effect*, pp. 117–132. Torus Press, Moscow (2005)
156. Basevich, V. Ya., Belyaev, A. A., Evlampiev, A. V., *et al*.: *Khimicheskaya Fizika* **21**(3), 58 (2002)
157. Atthasit, A., Doue, N., Biscos, Y., *et al*.: Influence of drop concentration on the dynamics and evaporation of a monodisperse stream of drops in evaporation regime. In: Roy, G. D., Frolov, S. M., Starik, A. M. (eds.) *Combustion and Atmospheric Pollution,* pp. 214–219. Torus Press, Moscow (2003)
158. Yang, J.-R., Wong, S. C.: *Combust. Flame* **132**, 475 (2003)
159. Frolov, S. M., Basevich, V. Ya., Posvianskii, V. S.: Limiting drop size and prevaporization degree required for spray detonation. In: Roy, G. D., Frolov, S. M., Shepherd, J. (eds.) *Application of Detonation to Propulsion*, pp. 110–119. Torus Press, Moscow (2004)
160. Basevich, V. Ya., Frolov, S. M., Posvianskii, V. S.: Existance conditions for stationary heterogeneous detonations. *Khimicheskaya Fizika* **24**(7), 60 (2005)
161. Basevich, V. Ya., Belyaev, A. A., Frolov, S. M.: *Chemical Physics Reports* **17**(9), 112 (1998)
162. Basevich, V. Ya., Belyaev, A. A., Frolov, S. M.: *Chemical Physics Reports* **17**(10), 71 (1998)
163. Evlampiev, A. V., Frolov, S. M., Basevich, V. Ya., *et al*.: *Chemical Physics Reports* **20**(11), 21 (2001)
164. Basevich, V. Ya., Belyaev, A. A., Brandstaetter, W., *et al*.: *Combustion Explosions Shock Waves* **30**(6), 15 (1994)
165. Basevich, V. Ya., Frolov, S. M., Posvianskii, V. S., *et al*.: *Khimicheskaya Fizika* **24**(5), 71 (2005)
166. Takei, M., Kobayashi, H., Niioka, T.: *Int. J. Microgravity Res. Appl. Microgravity Sci. Technol.* **1(**3), 184 (1993)
167. Niioka, T., Kobayashi, H., Mito, D.: In: *Proc. IVTAM Symp. Mechanics and Combustion of Droplet and Sprays Proc.,* pp. 367–377. Tainan (1994)
168. Roy, G. D., Frolov, S. M., Borisov, A. A., Netzer, D. W.: *Progr. Energy Combust. Sci.* **30**, 545–672 (2004)
169. Borisov, A. A., Komissarov, P. V., Kulikov, A. V., *et al*.: *Chemical Physics Reports* **17**(3), 49 (1998)
170. Frolov, S.M., Scripnik, A. A., Kavtaradze, R. Z.: Modeling of Diesel spray ignition. In: Roy, G. D., Frolov, S. M., Starik, A. M.: *Combustion and Atmospheric Pollution*, pp. 220–227. Torus Press, Moscow (2003)
171. Scripnik, A. A., Frolov, S. M., Kavtaradze, R. Z., *et al*.: *Khimicheskaya Fizika* **23**(1), 54 (2004)